Journal of Rock Mechanics and Geotechnical Engineering 18 (2026) 3654–3674

Contents lists available at ScienceDirect

Journal of Rock Mechanics and Geotechnical Engineering

journal homepage: www.jrmge.cn

Full Length Article

Thermo-mechanical analysis of fine-grained marble under cyclic temperature treatment and multilevel stress disturbances

Yu Song [a], Shengqi Yang [b,*], Kesheng Li [a,**], Yue Li [c], De'an Zheng [c], Yanhua Huang [c]

[a] State Key Laboratory of Intelligent Construction and Healthy Operation and Maintenance of Deep Underground Engineering, China University of Mining and Technology, Xuzhou, 221116, China
[b] State Key Laboratory of Intelligent Deep Metal Mining and Equipment, School of Civil Engineering, Shaoxing University, Shaoxing, 312000, China
[c] School of Mechanics and Civil Engineering, China University of Mining and Technology, Xuzhou, 221116, China

A R T I C L E I N F O

Article history:
Received 24 January 2025
Received in revised form
2 June 2025
Accepted 10 June 2025
Available online 22 September 2025

Keywords:
Thermal cycling
Multi-level fatigue
Nuclear magnetic resonance
Nanoindentation
Damage constitutive equation

A B S T R A C T

Thermal cycling and stress fatigue are recognized as principal factors that induce the Kaiser effect of rock in deep earth rock engineering. Nevertheless, existing scholarly investigations about the mechanical properties of rocks subjected to the synergistic effects of these perturbations have remained insufficient. In this study, conventional triaxial compression tests, multistage equal-amplitude fatigue (MEF) and multistage variable-amplitude fatigue (MVF) tests were conducted on marble subjected to different numbers of thermal cycles, integrated with nuclear magnetic resonance (NMR) and depth-sensing indentation (DSI) micro-monitoring methods, and the rock constitutive equation was established from the perspective of statistical microscopic damage. The results indicated that the increasing number of thermal cycles significantly weakened the physical and mechanical properties of marble, as evidenced by degradations in strength, deformation, and energy parameters. The reversible deformation evolutions of the rock under two stress paths were diametrically opposed. DSI results revealed that the microcellular mechanical parameters of hornblende and dolomite exhibited greater variability, although both conform to Weibull distribution functions. Additionally, NMR analysis showed that the porosity of the marble was 1.6% initially and increased to 3.3%, 4.1%, 5.8%, and 10.9% after 2, 4, 6, and 8 thermal cycles, respectively. The coupled thermal-mechanical damage constitutive model can effectively describe the deformation behavior of marble under complex perturbations, with distribution parameters m_0 and T_0 decreasing linearly with the number of thermal cycles.

1. Introduction

Hot dry rock (HDR), a category of geothermal resource, consists of high-temperature rock formations generally exceeding 200 °C, which located at depths of several kilometers and contain negligible subsurface fluid. Recent advancements in engineered geothermal technologies have propelled HDR into the spotlight as a pivotal renewable energy alternative (Williamson et al., 2001; White et al., 2018; Khatib, 2012; Yan et al., 2024).

Several advanced methods, including enhanced geothermal systems (EGS) and downhole heat exchanger systems (Balbay and Esen, 2010; Huang et al., 2018), were proposed to extract the energy in HDR. Some noteworthy differences have been found in these methods, such as energy conversion efficiency, the use of enclosed systems, the requirement for external driving mechanisms, and the number and configuration of heat transfer wells constructed (Templeton et al., 2014; Ebeling et al., 2017; Li et al., 2024). However, there are several consistent characteristics across them: (1) The temperature experienced by the wellbore and surrounding rock fluctuates cyclically (Riahi et al., 2019; Villarreal et al., 2021); (2) Cyclic loads from drilling machinery inevitably cause disturbances to the wellbore and surrounding rock (Sheng et al., 2020; Zhong et al., 2023); (3) The stability of the wellbore is crucial for determining the efficiency of heat extraction (AbuAisha et al., 2016). Therefore, investigating the thermal-mechanical behaviors of HDR under repeated external disturbances and cyclic temperature fluctuations is crucial for maintaining wellbore stability.

* Corresponding author.
** Corresponding author.
E-mail addresses: yangsqi@hotmail.com (S. Yang), likesheng@cumt.edu.cn (K. Li).
Peer review under responsibility of Institute of Rock and Soil Mechanics, Chinese Academy of Sciences.

https://doi.org/10.1016/j.jrmge.2025.06.042
1674-7755/

Over the past decades, the investigation of physical and mechanical properties of rocks exposed to high temperatures has been a well-researched field. Degradation of typical rock properties at elevated temperatures primarily manifests as reductions in strength, elastic modulus, fracture toughness, wave velocity, and stiffness, while simultaneously increasing porosity and permeability (Zhang et al., 2001, 2015; Liang et al., 2006; Yin et al., 2012; Chen et al., 2021; Luo et al., 2024). Classical findings have been adapted to assess high-temperature rock engineering. Laboratory experiments and microscopic analysis demonstrate that rocks begin to lose bound water at temperatures exceeding 200 °C, with structural water release occurring between 300 °C and 500 °C (Yang et al., 2014; Gao et al., 2024). When temperatures surpass 400 °C, significant chemical transformations occur, including recrystallization, clay mineral decomposition, and the α-β quartz transition at 573 °C (Li et al., 2020). Additionally, carbonate mineral decomposition is observed above 700 °C (Ma et al., 2023). In summary, the above findings underscore the necessity for rigorous evaluation of high-temperature rock formations to mitigate engineering risks.

In deep geothermal engineering with the depth less than 10 km and the temperatures below 300 °C, significant controversies persist regarding the thermal regulation mechanisms governing the mechanical behavior of the surrounding rock. Although substantial mineral phase transitions and chemical alterations are absent from this temperature range interval (Chen et al., 2012; Li et al., 2023), as illustrated in Fig. 1, marble and granite may exhibit diametrically opposed thermal responses within this “moderate” interval. The coexistence of thermal strengthening and weakening effects indicates that the moderateness of the temperature range is unable to unilaterally dictate mechanical behavior; instead, it arises from the nonlinear coupling between thermal-mechanical paths (e.g., heating rates, cyclic loading) and the native rock structure (porosity, mineral distribution). The contradictory phenomena originate from three competing mechanisms: (1) Dualistic thermal expansion effects: Mineral grain expansion can compact native pores (strengthening) or induce intergranular tensile stress due to heterogeneous expansion (weakening), with dominance governed by grain contact morphology and thermal loading rates (Kang et al., 2021; Wong et al., 2022). (2) Competition between thermal stress accumulation and relaxation: Slow heating facilitates stress relaxation, promoting grain rearrangement and densification, whereas rapid thermal cycles (e.g., abrupt temperature changes in geothermal wells) generate transient stresses exceeding damage thresholds, triggering microcrack nucleation (Huang et al., 2018; Tian et al., 2022). (3) Threshold effects of native defects: Initial porosity and microcrack density define critical thresholds for thermal damage (Wong et al., 2020). Below these thresholds, strengthening dominates; above them, weakening cascades are activated. While existing studies have elucidated the roles of mineral composition (Waragai, 2022) and static thermal loading (Yang et al., 2022), systematic understanding remains lacking for the coupling mechanisms between non-steady thermal-mechanical paths (e.g., thermal cycling, abrupt thermal gradients) and complex stress conditions prevalent in practical engineering scenarios.

In recent years, the mechanical behavior of rocks subjected to high-temperature treatment under cyclic loading conditions has been investigated, three aspects have been summarized: (1) Involving the study objects, sandstone, granite, marble, limestone, rock salt and granodiorite have been intensively chosen (Shkuratnik et al., 2020; Sepúlveda et al., 2020; Meng et al., 2021; Xiao et al., 2021a,b; Hu et al., 2023; Song et al., 2024). (2) Involving the study methods, mainly ranged from laboratory methods including uniaxial cyclic loading tests, triaxial cyclic loading tests and graded cyclic loading tests, numerical simulation by utilizing finite element and discrete element methods and theoretical model containing damage constitutive and elastoplastic constitutive models (Meng et al., 2022; Luo and He, 2022). (3) Involving the study content, the characteristics of permeability evolution, crack types and failure modes, stress-strain curves, strength and deformation characteristics, acoustic emission behavior and energy evolution characteristics (Meng et al., 2021, 2022; Tian et al., 2021; Luo and He, 2022; Sun et al., 2024) have been hot topics in the study on coupling of high temperature-cyclic loading test. The above studies have provided insights into the engineering properties of high-temperature rocks in deep underground environments. However, the rock around geothermal well often experiences mechanical disturbances with frequencies that exceed those used in the cyclic loading and unloading experiments conducted. Additionally, the temperature of the surrounding rock can fluctuate significantly within a mild range due to periodic heat exposure. The effects of these multiple thermal cycles, as well as the multi-stage stress disturbance remain unclear. Therefore, it is essential to investigate the physical and mechanical properties of rocks subjected to multilevel fatigue loads after thermal cycles. Additionally, there is a lack of comprehensive damage constitutive models to describe the mechanical behavior of rock under multi-stage fatigue loading after high-temperature treatment, with most existing research focusing only on single-stage fatigue scenarios (Zhou et al., 2017; Liu et al., 2023; Shi et al., 2024). Consequently, developing a damage constitutive model that accounts for

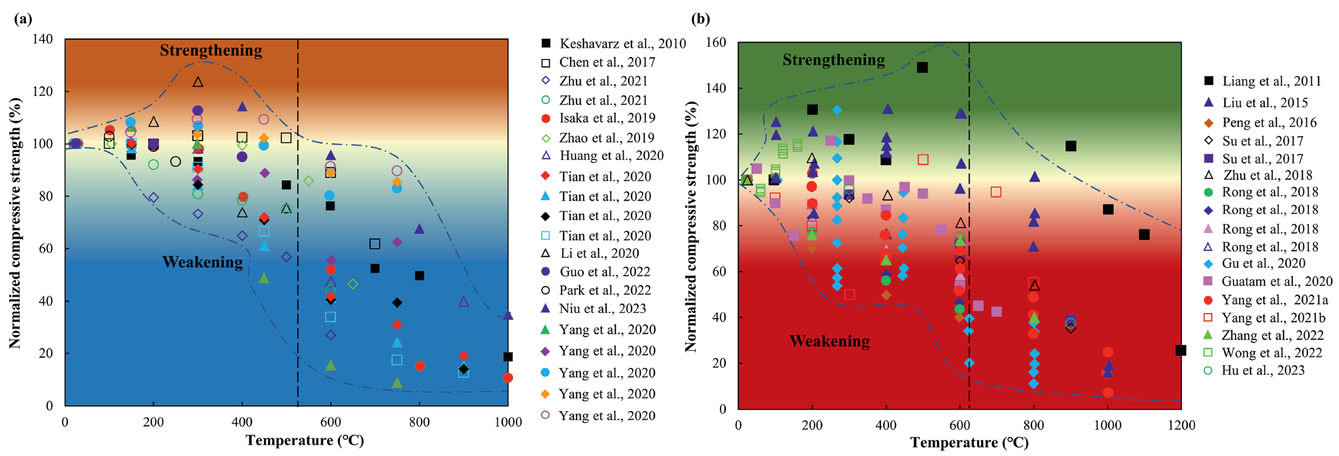

Fig. 1. Distribution of normalized compressive strength of common rocks with increasing temperature (Song et al., 2024): (a) Granite and (b) Marble.

high-temperature multi-stage fatigue loads is of significant importance.

In this study, a critical temperature ranging from mild to high temperatures (350 °C) was selected, and fine-grained marbles were subjected to different thermal cycling treatments. Uniaxial compression tests (UCT) and multi-stage fatigue tests were conducted to assess changes in deformation, strength, and failure characteristics induced by high-temperature damage. The energy evolution of the samples under cyclic loading, subjected to different number of thermal cycling, was then analyzed. NMR and DSI tests were employed to quantitatively examine the effect of different thermal cycles on the softening and damage of the rocks from a microscopic perspective. Finally, based on both macro- and micro-scale experimental results and meso-scale statistical damage theory, a constitutive model for rock damage under multi-stage fatigue conditions following cyclic thermal treatment was established.

2. Mechanical experimental methodology

2.1. Rock materials and mechanical experimental system

The test material for this study was taken from a complete piece of marble in Guangxi Province, China, which appeared pure white overall. The samples were extracted from the same rock mass and then drilled into standard specimens measuring 50 mm × 100 mm. The X-ray diffraction (XRD) results indicated that the mineral composition of the marble was mainly dolomite (90.24%), with a small amount of hornblende (5.74%) and calcite (4.02%). The average density was about 2.687 g/cm^3.

The experimental system utilized a multifunctional electro-hydraulic servo-controlled rigid testing machine, specifically designed by MTS Corporation in the United States for rock and concrete experiments. This machine has a maximum compressive load capacity of 4600 kN, a maximum tensile force capacity of 2300 kN, and a maximum confining pressure of 140 MPa. It offers a testing accuracy of $\leq \pm 0.5\%$ and a frame stiffness of 10.5×10^9 N/m. The system is capable of generating various waveforms, including sine waves, triangular waves, square waves, and ramp signals.

2.2. Mechanical experimental procedure

The specimens were first heated to 350 °C with a rate of 3 °C/min to prevent non-uniformity deformation. When the temperature reached the specified value, a constant temperature was maintained for 4 h in order to ensure a consistent global temperature of the rock (as shown in Fig. 2). After thermal cycling, the specimens were removed from the muffle furnace (transfer time ≤1 min), quickly submerged in 25 ± 1 °C water (water volume ≥20 L), the height of the water surface exceeded the top of the specimen by 50 mm, and kept for 2 h to ensure that the internal and external temperatures were consistent. After cooling, the specimens were placed in a cool place to dry naturally, and then transferred to a 50 °C drying oven to dry for 24 h. The cooling water should be changed every time to maintain the constant temperature. Several cycles of thermal treatments, 0, 2, 4, 6, and 8, were performed as described above.

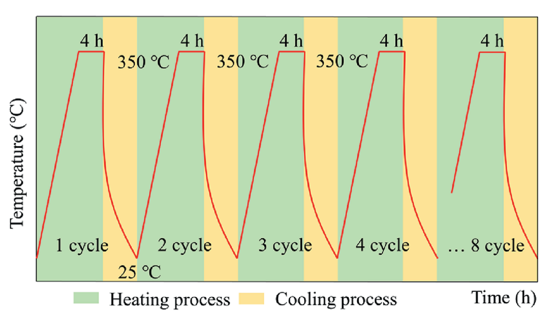

Fig. 2. Schematic diagram of cyclic heating treatment.

The mechanical test programs were divided into uniaxial compression test and fatigue test, and the uniaxial compression test was loaded with a stress control of at a rate of 5 MPa/min. The fatigue loading schematic is shown in Fig. 3, a total of two fatigue schemes were designed, one is the MVF loading scheme, specifically, the lower limit was maintained at 5 MPa, and the initial stage was loaded to the upper limit of the first fatigue stage (10 MPa) at a rate of 5 MPa/min by the stress control after the specimen had been preloaded at 1 MPa, after that, fatigue loading was carried out by the sine wave with a frequency of 0.25 Hz, a total of 40 cycles were loaded in 160 s, and each stage was repeated by increasing the upper limit with 5 MPa until the specimen was damaged. On the other hand, the MEF loading scheme was designed in parallel, as shown in Fig. 3b, in which only the lower limit of each stage was modified in order to maintain its amplitude at 5 MPa compared to the previous scheme.

3. Experimental results

3.1. Analysis of stress-strain curves

Fig. 4 illustrates the stress-strain curves obtained from the uniaxial compression tests of marble subjected to varying numbers of thermal cycles. As detailed in Table 1, the average mass damage rates of the marble are 0.189 ‰, 0.303 ‰, 0.548 ‰, and 1.547 ‰ corresponding to 2, 4, 6, and 8 thermal cycles, respectively. Concurrently, the peak uniaxial strength decreases significantly from 49.11 MPa with 0 thermal cycles to 19.01 MPa with 8 thermal cycles. The most substantial reductions in peak strength occur between 0 and 2 thermal cycles and between 2 and 4 thermal cycles. Additionally, the peak axial strain and peak lateral strain initially increase and then decrease with the number of

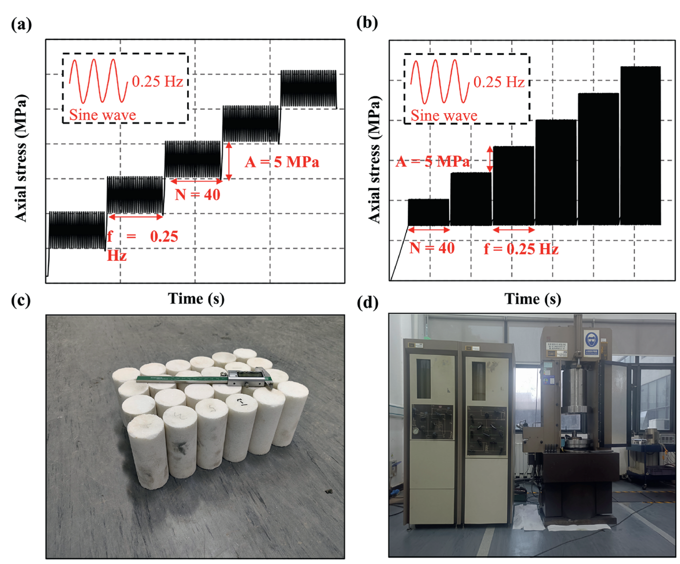

Fig. 3. Schematic diagrams of two fatigue loading schemes: (a) MVF scheme and (b) MEF scheme.

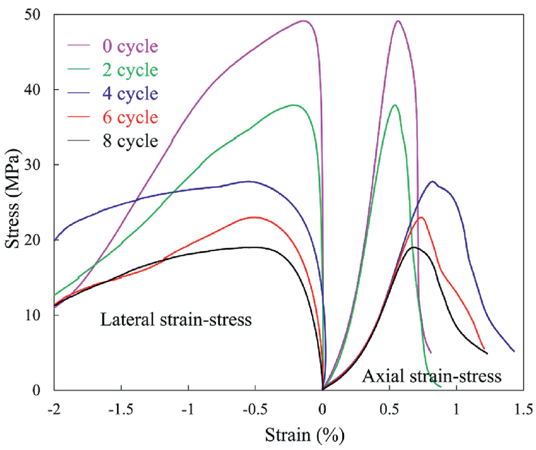

Fig. 4. Uniaxial compressive stress-strain curves of marble subjected to varying numbers of thermal cycles.

thermal cycles. The modulus of elasticity consistently declines to 13.06 GPa, 9.95 GPa, 5.41 GPa, 5.09 GPa, and 4.14 GPa, respectively. These findings indicate that thermal cycles at 350 °C significantly affect the physical and mechanical properties of marble, and change it from a quasi-brittle to a more ductile state.

The stress-strain curves of marble subjected to varying numbers of thermal cycles, obtained from MVF and MEF tests, are presented in Figs. 5–9. These curves reveal that the fatigue behavior of marble without thermal treatment follows the classical four stages: pore compaction stage, elasticity stage, accumulation of plastic deformation stage, and macro failure stage. Both MVF and MEF hysteresis curves exhibit a “sparse-dense-sparse” pattern as the stress level increases. However, with more thermal cycles, the irreversible displacement in the hysteresis loop gradually increases. This effect becomes particularly pronounced after six thermal cycles.

Focusing on the single stress level stage (with a magnified view provided in the figures), it is evident that the curve demonstrates a “sparse-dense” pattern, indicating that damage due to cyclic stresses is primarily concentrated in the initial cycle of loading. As stress levels continue to increase, the hysteresis loop gradually transforms into two distinct patterns: “dense-sparse” and “sparse-dense-sparse.” This indicates that damage induced by high-level stress perturbations has exceeded the threshold, leading to rapid accumulation of damage and progressive failure of the specimen.

Besides, Fig. 5 displays the volumetric stress-strain curves of marble subjected to varying numbers of thermal cycles under two stress paths. In the MVF condition, the volumetric stress-strain curves overlapped during the pore compaction and volume expansion stages. Under MEF condition, this phenomenon can be

Table 1
Physical and mechanical parameters of uniaxial compression of marble subjected to varying numbers of thermal cycles.

Samples	Q_{bh} (g)	Q_{ah} (g)	R_Q (‰)	σ_p (MPa)	ε_{ap} (%)	ε_{lp} (%)	E (GPa)
0 cycle	529.08	529.08	0	49.11	0.56	0.11	13.06
2 cycles	527.84	527.74	0.189	37.95	0.54	0.19	9.95
4 cycles	527.34	527.18	0.303	27.78	0.82	0.52	5.41
6 cycles	529.13	528.84	0.548	23	0.74	0.49	5.09
8 cycles	529.92	529.1	1.547	19.01	0.69	0.45	4.14

Note: Q_{bh} presents the quality of marble before heat treatment; Q_{ah} presents the quality of marble after heat treatment; R_Q is the quality loss ratio; σ_p presents the peak strength of UCT; ε_{ap} presents the peak axial strain of UCT; ε_{lp} presents the peak lateral strain of UCT; E is the elastic modulus.

observed more clearly. Specifically, when stress levels are low, volumetric strain gradually increases. As stress levels rise and the marble enters the elastic stage, the hysteresis loops become progressively denser. Upon entering the plastic damage stage, volumetric strain increases in the opposite direction. Additionally, as the number of thermal cycles increases, the volumetric strain of marble decreases significantly. Specifically, the peak volumetric strains of marble under MVF stress conditions at 0, 2, 4, 6, and 8 thermal cycles are 0.25%, 0.63%, 0.73%, 0.8%, and 1.81%, respectively. Under MEF stress conditions, these values are 0.15%, 0.25%, 0.34%, 0.51%, and 0.72%. It can be observed that the volumetric strain of marble under MVF stress conditions is significantly greater than that under MEF stress conditions.

3.2. Characteristics of deformation

3.2.1. Deformation analysis

To explore the effects of the number of thermal cycles and different stress paths on the deformation behavior of marble, the strains corresponding to the maximum and minimum stress levels in each cyclic curve are extracted and plotted in Figs. 10 and 11. And the reversible deformation for each cycle is recorded, which is calculated as the difference between the deformations at the highest and lowest stress levels within each cycle.

It is well known that rocks can hardly realize stable fatigue during fatigue due to the existence of internal defects, and their irreversible deformation will continue to increase with the increase of the number of cycles or the increase of the stress level. As shown in Fig. 10, when the stress level is low, the strain development at each stage can be mainly divided into two stages, i.e., the initial deformation stage and the uniform deformation stage. With the increase of stress level, the strain evolution shows typical initial deformation, uniform deformation and accelerated deformation stages with obvious rheological behavior.

As the number of thermal cycles increases, the total number of fatigue stages in the marble decreases systematically, transitioning from a multi-stage progressive damage process to a single-stage destabilization mode dominated by accelerated rheological flow. The experimental results under the MVF stress path (Figs. 10 and 11) show that, as the number of thermal cycles increases from 0 to 8, the corresponding fatigue life decreases sequentially from 324 cycles (0 heat treatments) to 83 cycles (8 heat treatments), and similarly the corresponding fatigue life decreases sequentially from 362 cycles (0 heat treatments) to 101 cycles (8 heat treatments) under the MEF path. This phenomenon suggests that prolonged thermal cycling induces a transition in the marble's strain response, shifting from multi-stage elastic-plastic coupling state to accelerated rheological stage dominated by residual strain accumulation.

In addition, an interesting phenomenon is observed: the reversible deformation obtained by MVF increases stepwise with the number of cycles, whereas that of MEF decreases stepwise. The former trend can be attributed to the progressive rise in stress levels, which directly correlates with higher strain at elevated stresses. Conversely, the MEF results exhibit an inverse pattern. Due to its smaller loading amplitude compared to MVF, the rock structure accumulates damage continuously with increasing stress levels, yet the elastic energy stored internally cannot be fully released. It results in enhanced macroscopic stiffness, causing the reversible strain to decline progressively. Notably, the strain reduction induced by elastic strengthening outweighs the strain increase from damage and stress-level rise. To further elucidate this mechanism, Fig. 17 statistically compares the total elastic energy percentages of marble under both loading modes after thermal cycling. The data reveal that MEF consistently retains

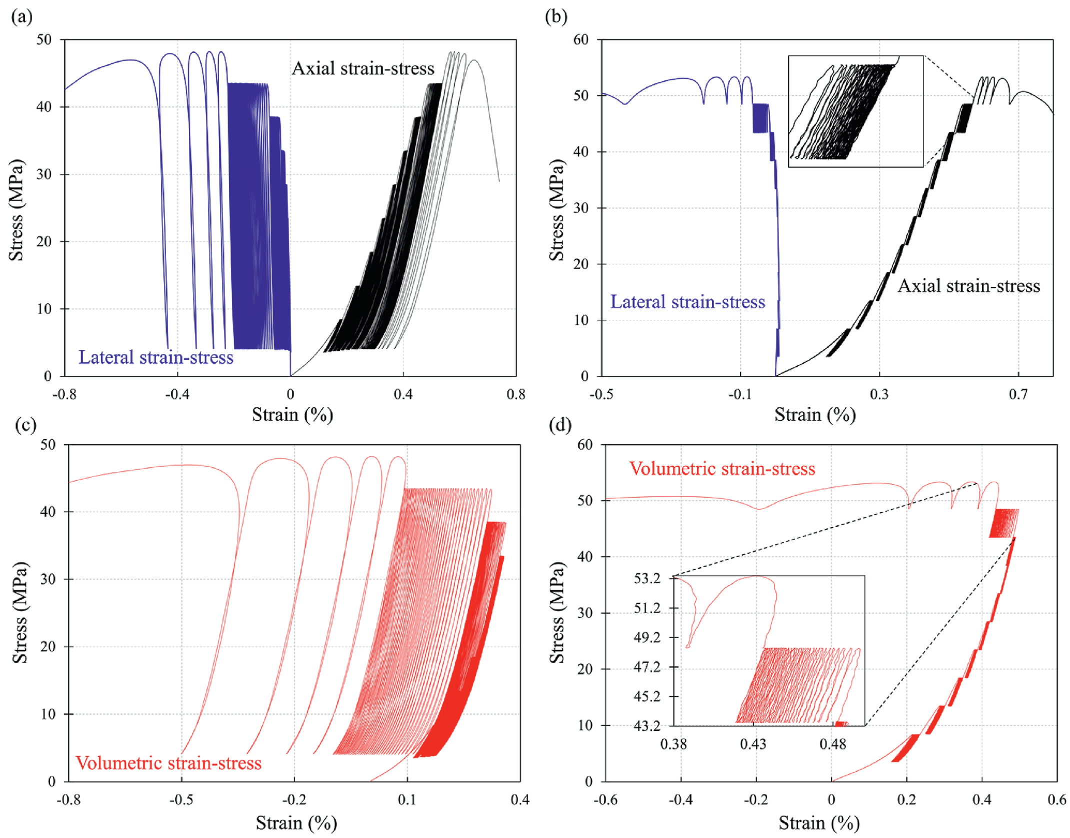

Fig. 5. Stress-strain curves of marble without thermal treatment: (a–b) are axial and lateral stress-strain curves of MVF and MEF, respectively, and (c–d) are volumetric stress-strain curves of MVF and MEF, respectively.

higher elastic energy proportions (98.4%, 95.5%, 93.5%, 91.9%, and 88.9% for 0, 2, 4, 6 and 8 thermal cycles) than MVF (95.3%, 91.9%, 90.9%, 85.9%, and 85.3%). This disparity suggests that MEF's smaller amplitude generates an energy buffering effect: its energy system maintains superior elastic storage capacity, ensuring that damage-induced strain increments are always suppressed by elastic strengthening.

3.2.2. Secant modulus analysis

In order to compare the effects of different numbers of thermal cycles and different stress paths on the dynamic modulus of marble, the secant modulus of the curves for the loading phase of each cycle is extracted, while the number of cycles is normalized to facilitate the comparison, as shown in Fig. 12.

It can be seen that for both the MVF and MEF stress paths, the secant modulus increases in a stepwise manner as the cyclic process increases, with the secant modulus of a single stage first increasing sharply and then decreasing gradually. And it is observed that the secant modulus of MFE is larger than that of MVF as a whole, which is consistent with the phenomenon described in Section 3.2.1. In addition, the secant modulus decreases substantially with increasing thermal cycles, and this reduction gradually attenuates as the cycling process continues.

Given the small magnitude of change in the secant modulus of marble during a single cyclic stage, it is important to focus on the evolution observed in the secant modulus during the first cycle of each stage. To illustrate this, the data are extracted and plotted in Fig. 13. It can be observed that the secant modulus obtained from the MVF test exhibits logarithmic growth patterns when the number of thermal cycles is less than or equal to 2, while it shows linear growth patterns at 4, 6, or 8 thermal cycles. In contrast, the secant modulus obtained from the MEF test presents logarithmic growth patterns when the number of thermal cycles is less than or equal to 4, and changes to linear growth patterns when the number of thermal cycles exceeds 4. Additionally, the slopes of the growth trend decrease as the numbers of thermal cycles increase.

3.3. Characterization of energy evolution

The fields of rock mechanics often reflect the deformation damage process characteristics and microscopic crack extension of rocks through energy, which is not only closely related to rock strength, but also can be used to propose damage constitutive model based on dissipated energy changes occurring in rock mass units. Therefore, in this paper, the energy evolution of marble in sabotage is calculated with different numbers of thermal cycles and various stress paths, and the principle of calculation is referred to Fig. 14. According to the first law of thermodynamics, the dissipated energy, elastic strain energy and total input energy can be obtained by calculating the area of the stress-strain curve envelope, respectively:

$$U_T = U_e + U_d \tag{1}$$

where U_T is the total input energy, U_e represents the elastic strain energy and U_d indicates the dissipation energy of marble during multilevel constant-amplitude fatigue loading tests.

As shown in Fig. 14, for any hysteresis loop consisting of loading and unloading curves, the corresponding energy can be obtained by means of curve integration:

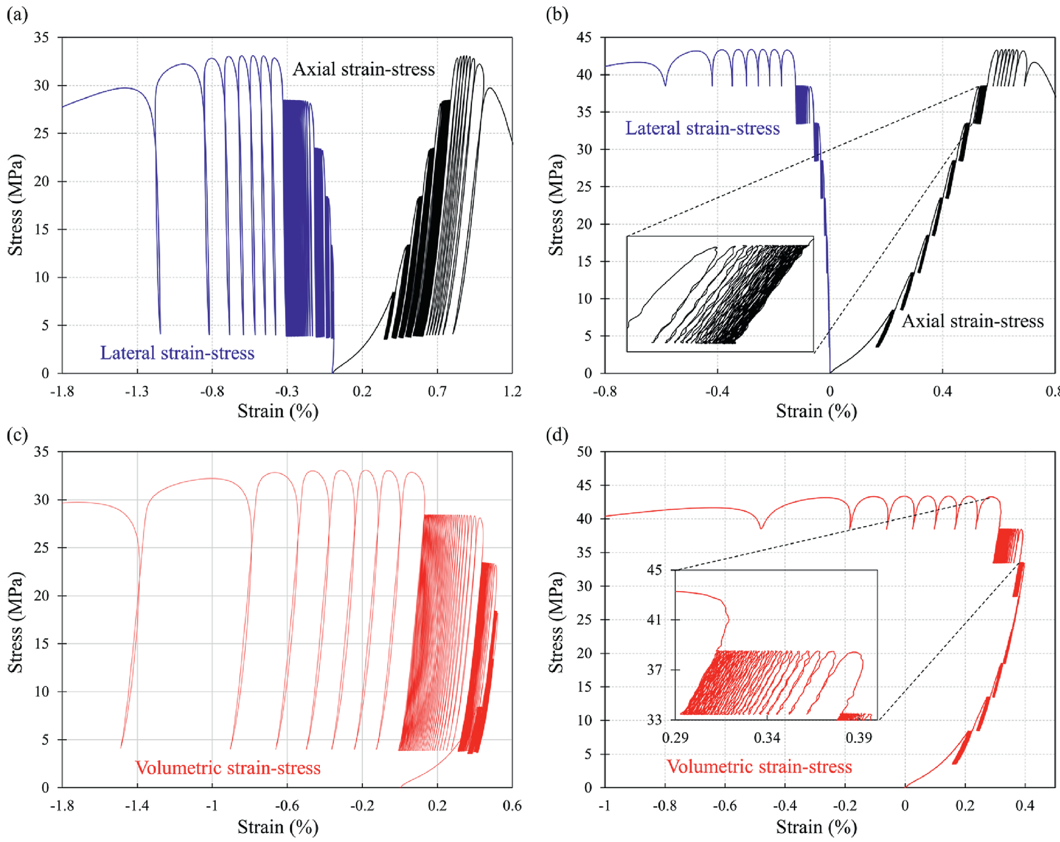

Fig. 6. Stress-strain curves of marble subjected to 2 thermal cycles: (a–b) are axial and lateral stress-strain curves of MVF and MEF, respectively, and (c–d) are volumetric stress-strain curves of MVF and MEF, respectively.

$$U_T = S_{ABCF} = \int_{\varepsilon_{n-1}}^{\varepsilon_{m-1}} \sigma_L d\varepsilon \tag{2}$$

$$U_e = S_{CDEF} = \int_{\varepsilon_n}^{\varepsilon_{m-1}} \sigma_U d\varepsilon \tag{3}$$

$$U_d = U_T - U_e = \int_{\varepsilon_{n-1}}^{\varepsilon_{m-1}} \sigma_L d\varepsilon - \int_{\varepsilon_n}^{\varepsilon_{m-1}} \sigma_U d\varepsilon \tag{4}$$

where σ_L and σ_U represent the loading stress and unloading stress in the hysteresis loop, respectively. ε_{n-1} and ε_n indicate the strain at minimum stress level of the n-1-th and n-th hysteresis loop, respectively, and ε_{m-1} is the strain at maximum stress level of the n-th hysteresis loop.

Figs. 15 and 16 illustrate the densities of total, elastic and dissipated energy of the marble after different numbers of thermal cycles in the MVF and MEF tests. As the number of stress cycles increases, the total input energy and dissipated energy of individual stages exhibit an “L” shape, i.e., the energy of the first cycle always preserves the maximum, and then gradually decreases until it remains stable, which indicates that the damage is mainly concentrated in the first cycle. This phenomenon is more conspicuous with the increasing number of thermal cycles. In addition, the energy tends to increase in a stepwise manner as the number of stages increases. Comparing the two stress paths, the final dissipated energy of MVF is higher than that of MEF, while MEF always has a higher proportion of dissipated energy in the first cycle of each stage. Furthermore, under MEF stress path, the elastic energy shares of marble subjected to increasing thermal cycles are measured at 98.4%, 95.5%, 93.5%, 91.9%, and 88.9%, respectively. These values consistently exceed those observed under MVF stress path, which register at 95.3%, 91.5%, 90.9%, 85.9%, and 85.3%.

4. Microscopic inspection

4.1. Mechanical analysis of DSI

The previous analyses have revealed that cyclic thermal treatment at the critical temperature significantly affected the macromechanical behavior of fine-grained marble; however, the underlying damage mechanisms have remained unclear. To further investigate this, ten marble discs, each with a diameter of 10 mm and a thickness of 5 mm, were prepared, and DSI mechanical tests were conducted on hornblende and dolomite subjected to various thermal cycles, which constituted the majority of the marble. The constant depth indentation method was employed for these tests. A diamond indenter was applied at a rate of 20 nm/s, with a maximum indentation depth of 2000 nm. Upon reaching this maximum depth, the load was held for 10 s before gradually released at the rate of 20 nm/s.

To ensure the representativeness and statistical reliability of the test results, the selection of nine indentation test locations adhered to the following criteria: (1) Mineral distribution homogeneity control: the mineral composition of the sample surface was pre-characterized using polarized light microscope. Test points were exclusively selected within uniform regions where a single mineral phase (e.g., dolomite or hornblende) accounted for >95% of the composition, avoiding interference from mineral boundaries or cracks. (2) Spatial distribution strategy: a “3 × 3 grid

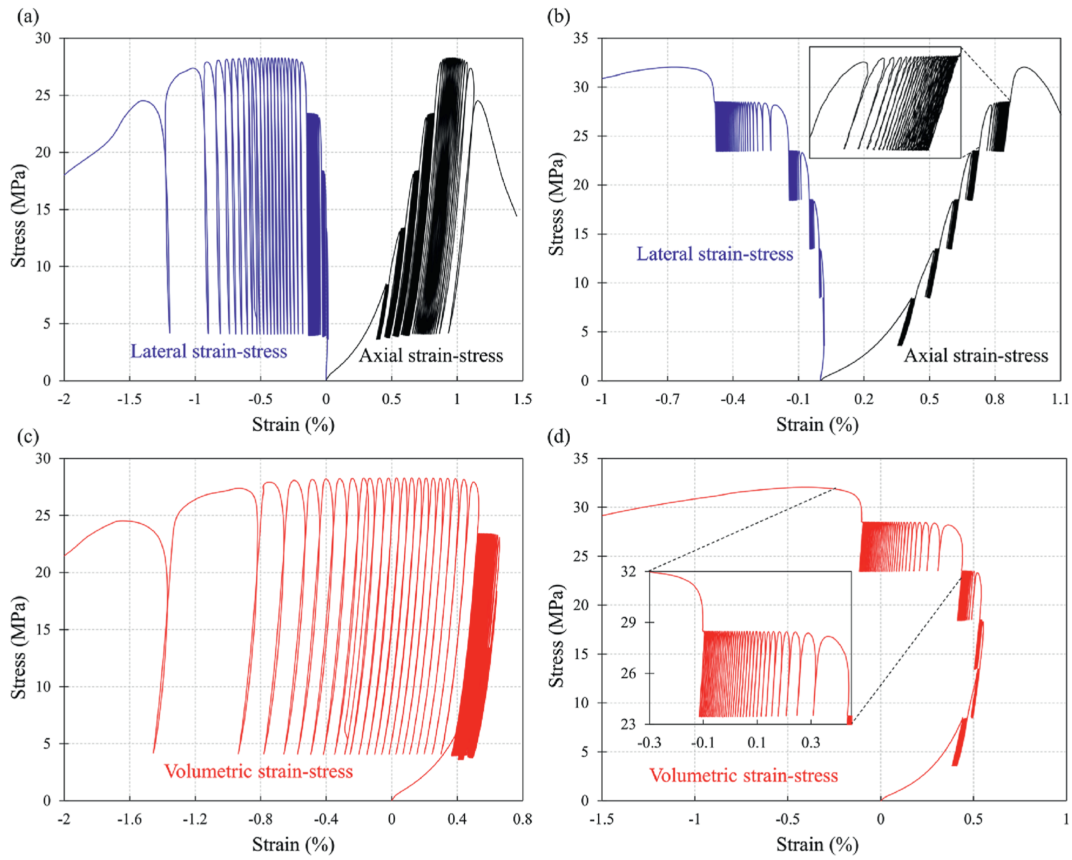

Fig. 7. Stress-strain curves of marble subjected to 4 thermal cycles: (a–b) are axial and lateral stress-strain curves of MVF and MEF, respectively, and (c–d) are volumetric stress-strain curves of MVF and MEF, respectively.

pattern" was applied to uniformly cover the sample surface (spacing ≥200 μm), eliminating errors caused by local defects or edge effects. (3) Statistical requirements: at least nine independent tests were conducted to mitigate the discreteness of micromechanical properties, with the mean value and standard deviation calculated (Liu et al., 2021).

Fig. 18 illustrates the DSI mechanical curves and microscopic observations of hornblende and dolomite subjected to various thermal cycles. Each mineral was tested nine times at different locations, revealing significant variability in the mechanical properties across different sites. It is worth noting that a few indentation results have an indentation depth of more than 2000 nm, which may be due to the insufficient surface roughness of the marble samples and the collapse of the mineral structure during the creep process. Nevertheless, the impact on the overall indentation results is negligible, as the errors due to these factors are less than 5% (<100 nm).

The strength characteristics of the microunits are found to be randomly distributed and discrete. As depicted in Fig. 19, the average strength, hardness, and elastic modulus for both hornblende and dolomite decrease with an increasing number of thermal cycles. Specifically, the average normal strengths of dolomite for 0 to 8 cycles are 222.49 mN, 184.93 mN, 104.65 mN, 65.56 mN, and 41.48 mN, respectively. For hornblende, these strengths are 177.53 mN, 138.31 mN, 124.50 mN, 101.60 mN, and 82.75 mN, respectively. The strength weakening observed in dolomite is more pronounced compared to dolomite, indicating that dolomite has a greater resistance to thermal cycling. The average hardness values for dolomite across the same cycles are 1.41 GPa, 1.21 GPa, 0.84 GPa, 0.48 GPa, and 0.37 GPa, while for dolomite they are 1.58 GPa, 1.00 GPa, 0.89 GPa, 0.88 GPa, and 0.52 GPa, respectively. Additionally, the average elastic modulus for dolomite decreases from 47.55 GPa to 12.15 GPa over the cycles, whereas for dolomite it ranges from 57.03 GPa to 20.60 GPa. In addition, Fig. 20 shows the probability distribution of peak intensities of hornblende and dolomite in different intensity ranges. It can be observed that their micro unit intensities are mainly concentrated in the range of 100–200 mN and followed the distribution pattern of probability functions.

In summary, the results of the DSI mechanical tests lead to the following conclusions: (1) The strength, hardness and elastic modulus of the microscopic units in the marble conform to a probabilistic random distribution, although the differences are significant, the average values have a representative implication, and are able to reflect the strength of their physical and mechanical properties. (2) Thermal cycling directly affects the physical and mechanical properties of the rock matrix with an obvious weakening effect. (3) The physical and mechanical properties of hornblende and dolomite exhibit generally identical behaviors under thermal cycling.

4.2. NMR results analysis

Previous studies have shown that high temperatures can induce thermal cracking, resulting in a reduction of mechanical properties and changes to the internal pore structure. To further investigate these effects, NMR analysis were performed on marble samples subjected to different numbers of thermal cycles. Following the thermal cycling treatment, the specimens were saturated with water using a vacuum saturation device. The pore

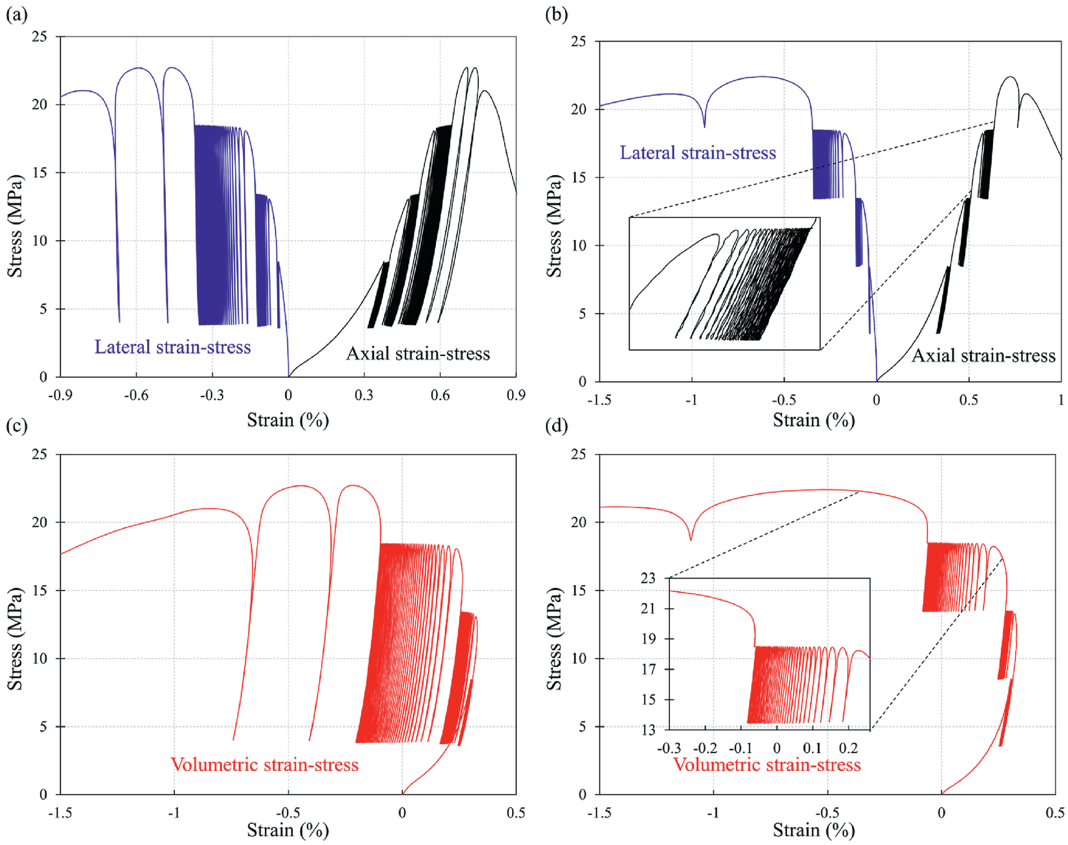

Fig. 8. Stress-strain curves of marble subjected to 6 thermal cycles: (a–b) are axial and lateral stress-strain curves of MVF and MEF, respectively, and (c–d) are volumetric stress-strain curves of MVF and MEF, respectively.

distribution was then assessed using an NMR microanalysis system. Signal intensity decay curves were obtained through the Carr-Purcell-Meiboom-Gill (CPMG) sequence, and pore volume occupancy at different scales was determined via numerical inversion.

The vertical axis of the T_2 spectral curve reflects the pore content corresponding to specific pore sizes. Based on previous research (Fan et al., 2024), marble pores were categorized into four types based on their size: micropores, small pores, medium pores, and large pores, arranged in increasing order of size. Fig. 20 presents the T_2 spectral curves of the marble, with four color-coded regions from left to right representing micropores, small pores, medium pores, and large pores, respectively. Specifically, the distribution of relaxation times corresponding to microscopic pores is in the range of $T_2 < 1$ ms, for small pores 1 ms $< T_2 <$ 5 ms, for medium pores 5 ms $< T_2 <$ 25 ms, and for large pores $T_2 >$ 25 ms. It is evident from Fig. 21a that the T_2 spectrum of marble exhibits a multi-peak distribution. Furthermore, as the number of thermal cycles increases, the T_2 spectrum of marble undergoes substantial changes. The porosity of marble subjected to 0, 2, 4, 6, and 8 thermal cycles is 1.6%, 3.3%, 4.1%, 5.8%, and 10.9%, respectively.

5. Coupled thermal-fatigue loading damage constitutive equation

5.1. Damage causation analysis

The damage mechanisms of marble under thermal-mechanical coupling are inherently complex. This study delineates two primary categories of damage: that resulting from thermal cycling and that induced by mechanical loading. As illustrated in Fig. 22, a range of influencing factors give rise to distinct physical and mechanical behaviors in marble. By integrating macro- and micro-scale experimental findings with established principles, a comprehensive synthesis of the phenomena associated with these factors is provided:

(1) Increasing porosity caused by thermal cycles: Based on the results of NMR tests, it can be seen that the porosity of marble increases gradually with the increasing number of thermal cycles, which will result in decreasing effective bearing area of marble.
(2) Elastic modulus evolution: The results of the DSI mechanical tests show that the average deformation modulus of the minerals inside the marble decreases after different numbers of thermal cycles. In addition, the elastic modulus increases gradually with the number of stages during fatigue loading.
(3) Increasing in plastic deviatoric strain due to monotonic loading: Many mechanical parameters can represent the damage during monotonic loading, such as axial strain, dissipation energy, etc. In this study, to simultaneously consider the deformation characteristics of marble in both axial and radial directions, the plastic deviatoric strain is selected as the damage variable for monotonic loading.

5.2. Derivation of coupled damage evolution function

5.2.1. Microcellular pore medium variation

The NMR results in Section 4.2 show that cyclic thermal

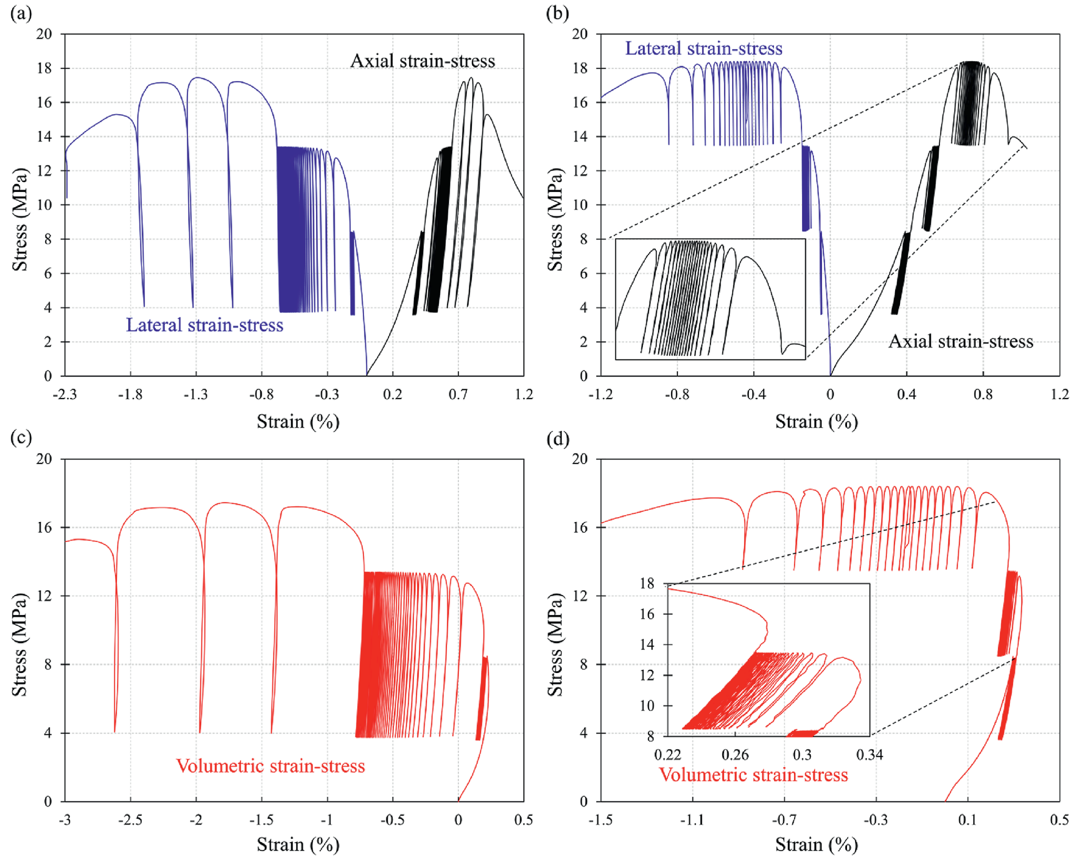

Fig. 9. Stress-strain curves of marble subjected to 8 thermal cycles: (a–b) are axial and lateral stress-strain curves of MVF and MEF, respectively, and (c–d) are volumetric stress-strain curves of MVF and MEF, respectively.

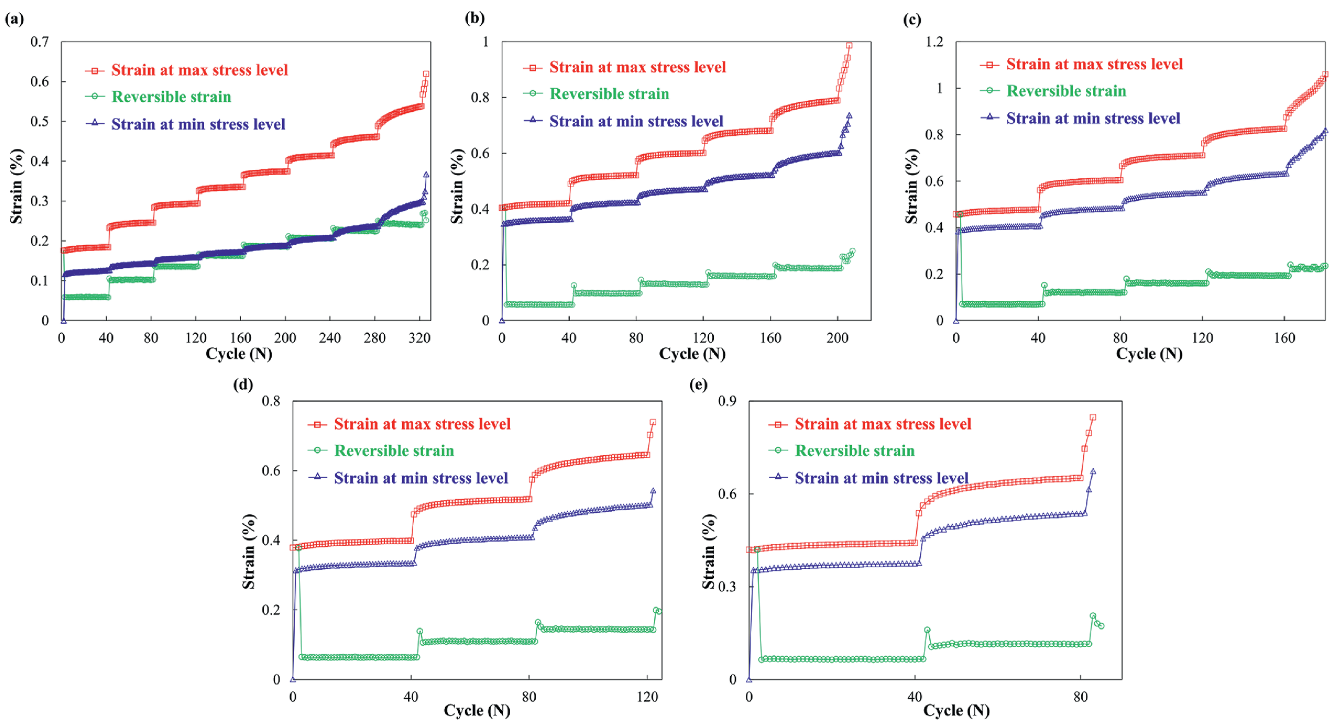

Fig. 10. Deformation of marble in the MVF test subjected to varying numbers of thermal cycles: (a–e) correspond to 0, 2, 4, 6, and 8 thermal cycling, respectively.

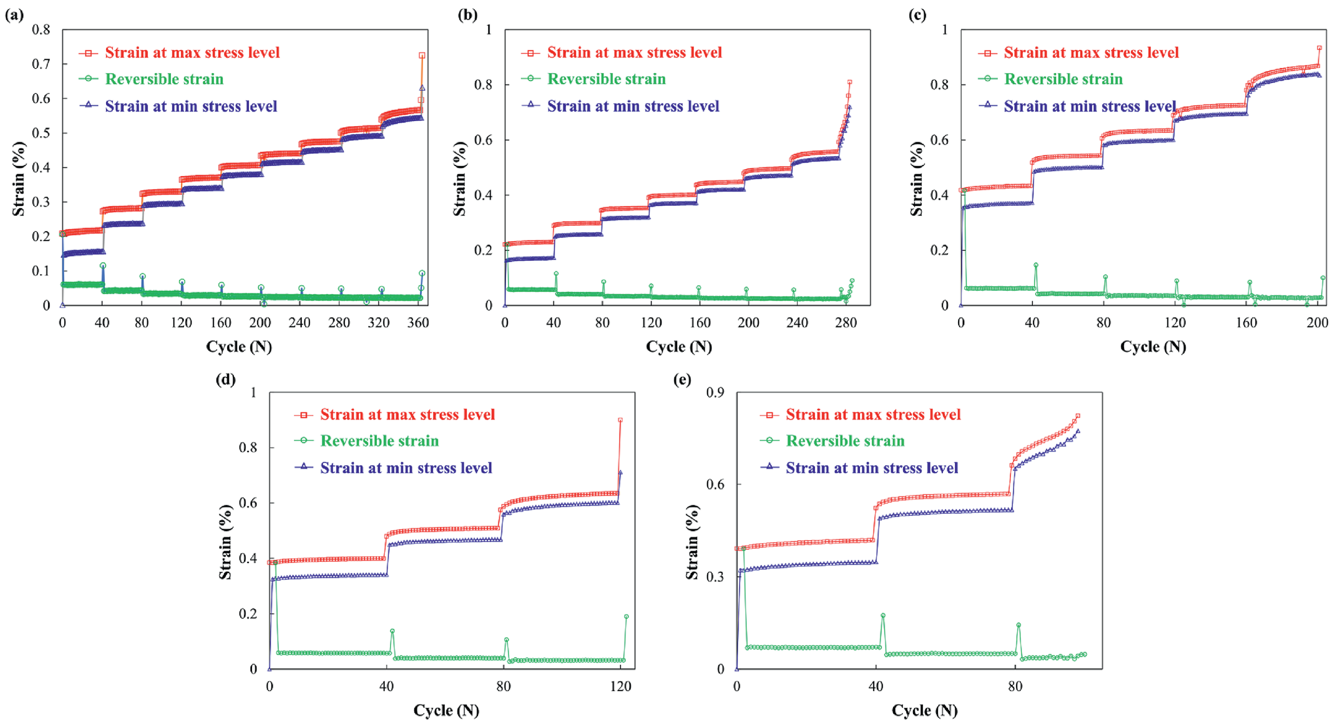

Fig. 11. Deformation evolution of marble in the MEF test subjected to varying numbers of thermal cycles: (a–e) correspond to 0, 2, 4, 6, and 8 thermal cycling, respectively.

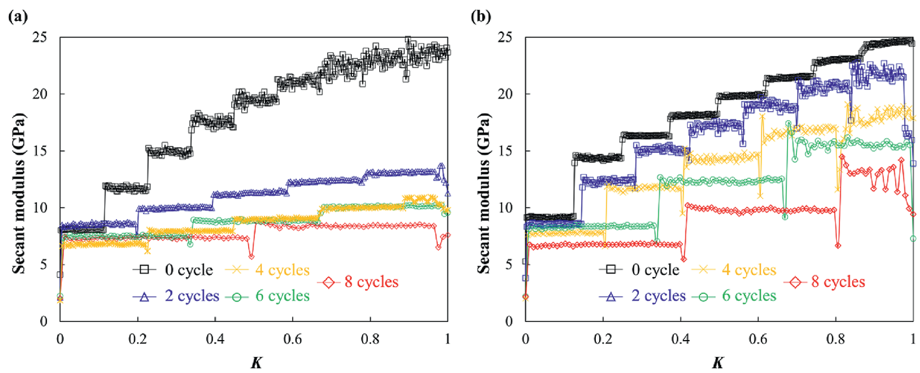

Fig. 12. Evolution of secant modulus of thermal shocked marble subjected to varying numbers of thermal cycles under different fatigue stress paths: (a) MVF and (b) MEF.

treatment at high temperatures induces significant porosity increase of marble, attributed to inhomogeneous thermal stresses that expand and squeeze crystal units to sprout both intragranular and transgranular cracks. However, during the initial and yielding phases of the mechanical tests, the pore structure within the rock undergoes a compaction stage and an expansion process, which subsequently lead to alteration of the accurate effective bearing area of the rock. Therefore, based on the mechanical condition of continuous medium, the representative volume element concept is proposed, and the damage intrinsic model is established (Ren et al., 2022). According to the derivation of Yao et al. (2023), the porosity e can be expressed as

$$e = \frac{e_0 - \varepsilon_v}{1 - \varepsilon_v} \tag{5}$$

where e_0 is the initial void ratio, and ε_v is the volume strain.

Eq. (5) is a method of calculating the pore ratio based on elastic cross sections, however, as the stress level rises and the number of fatigue times increases, the plastic deformation of the marble will continue to increase, resulting in Eq. (5) no longer being applicable. Therefore, a correction to the pore ratio for plastic deflection strain is usually quoted:

$$e = \left(1 + \frac{\gamma^d}{\gamma_m^d}\right)\left(\frac{e_0 - \varepsilon_v}{1 - \varepsilon_v}\right) \tag{6}$$

where γ^d represents the plastic deviatoric strain and γ_m^d represents the maximum plastic deviatoric strain.

5.2.2. Description of elastic modulus evolution

The results of the macro-mechanical tests show that the elastic modulus of marble exhibits different evolution patterns under different fatigue stress loading processes and numbers of thermal cycles. As shown in Figs. 12 and 13, the elastic modulus of heat-treated marble during fatigue can be expressed by the following equations:

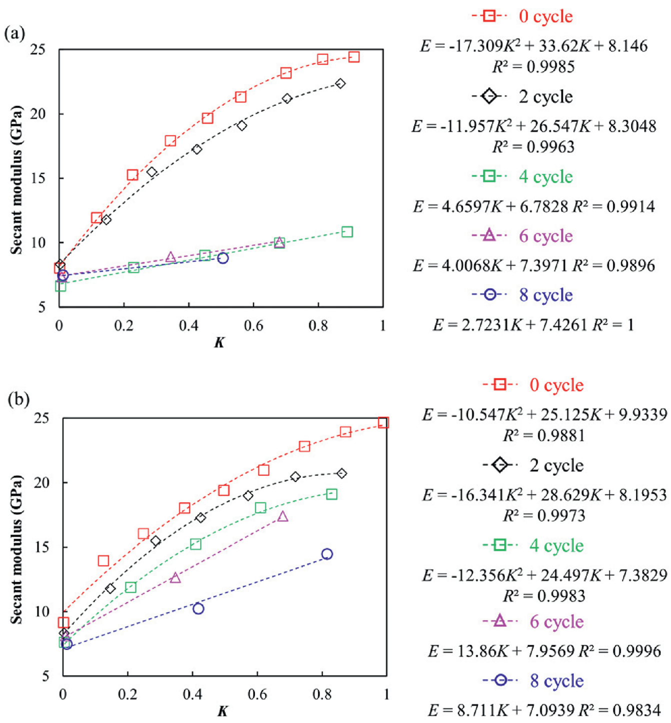

Fig. 13. Evolution curves of secant modulus of the first cycle of each phase of marble with normalized cyclic progression subjected to varying numbers of thermal cycles under two stress paths.

$$E_T = AK^2 + BK + C \tag{7}$$

$$K = \left[\frac{i}{N}\right] \Big/ L \tag{8}$$

where E_T is the elastic modulus of marble after heat treatment during the fatigue loading; K is the loading process parameter; A, B, C are the fit parameters; i represents the number of cycles; N is the total number of cycles at a stress level; and L is the total number of stages.

5.2.3. Description of mechanical damage

Based on the statistics of the DSI micro-mechanics results, the strength of the marble microunits is found to be random, conforming to the Weibull distribution, and its probability density function can be expressed as

$$P(T) = \frac{m_0}{F_0}\left(\frac{T}{T_0}\right)^{m_0-1} \exp\left[-\left(\frac{T}{T_0}\right)^{m_0}\right] \tag{9}$$

where T represents the micro-unit strength, which is a randomly distributed variable; m_0 and T_0 are the Weibull distributed parameters.

According to previous studies, the plastic deformation induced by monotonic loading during fatigue is considerable, thus, the randomly distributed variable is often defined as the plastic bias strain, and Eq. (9) is modified as (Yao et al., 2023):

$$P\left(\gamma^d\right) = \frac{m_0}{F_0}\left(\frac{\gamma^d}{T_0}\right)^{m_0-1} \exp\left[-\left(\frac{\gamma^d}{T_0}\right)^{m_0}\right] \tag{10}$$

Based on the continuous medium assumption, the number of damaged microunits within the marble is defined as N_d and the total number of microunits is defined as N, then their ratio is the damage variable:

$$D_m = \frac{N_d}{N} \tag{11}$$

where D_m is the damage variable of monotonic loading. Integrating the probability density function over a random interval yields the microporous damage number N_d:

$$N_d\left(\gamma^d\right) = \int_0^{\gamma^d} NP\left(\gamma^d\right) d\gamma^d = N\left\{1 - \exp\left[-\left(\frac{\gamma^d}{T_0}\right)^{m_0}\right]\right\} \tag{12}$$

The monotonic loading damage variable can be obtained by Eq. (11) and Eq. (12):

$$D_m = 1 - \exp\left[-\left(\frac{\gamma^d}{T_0}\right)^{m_0}\right] \tag{13}$$

The degree of damage during fatigue is often defined by the elastic modulus, dissipated energy, and maximum or minimum displacement, however, it is found through this study that these parameters are difficult to differentiate the properties of fatigue with different stress paths (e.g., MVF and MEF used in this paper). The reversible deformation per cycle is adopted in this study as the damage variable during fatigue loading, which is actually a hypothetical damage variable used to correct for the variability caused by the different loading methods, and in fact, the change in reversible deformation reflects the change in rock stiffness during fatigue. It can be expressed as

$$D_f = \sum_{i=1}^{n}\left(\frac{\varepsilon_{ri}}{\varepsilon_m}\right) \tag{14}$$

where D_f is the damage variable of fatigue loading; ε_{ri} is the axial reversible strain of ith cycle; ε_m represents the total axial reversible strain.

Coupled damage variables for monotonic and fatigue loading are obtained based on the Lemaitre strain equivalence hypothesis:

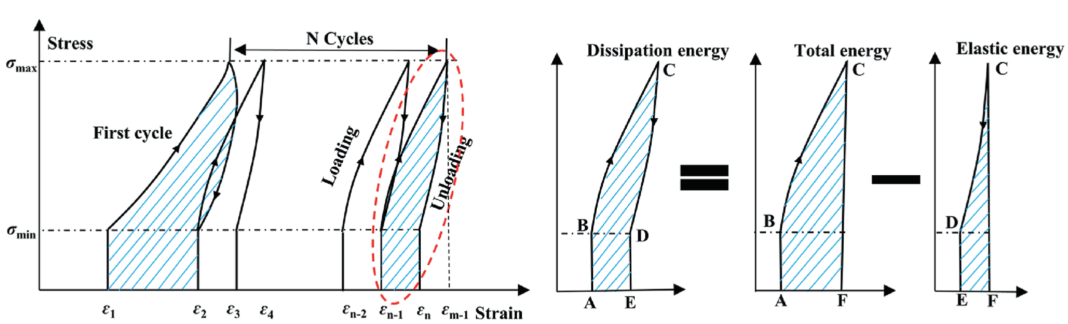

Fig. 14. Energy calculation schematic (Song et al., 2023).

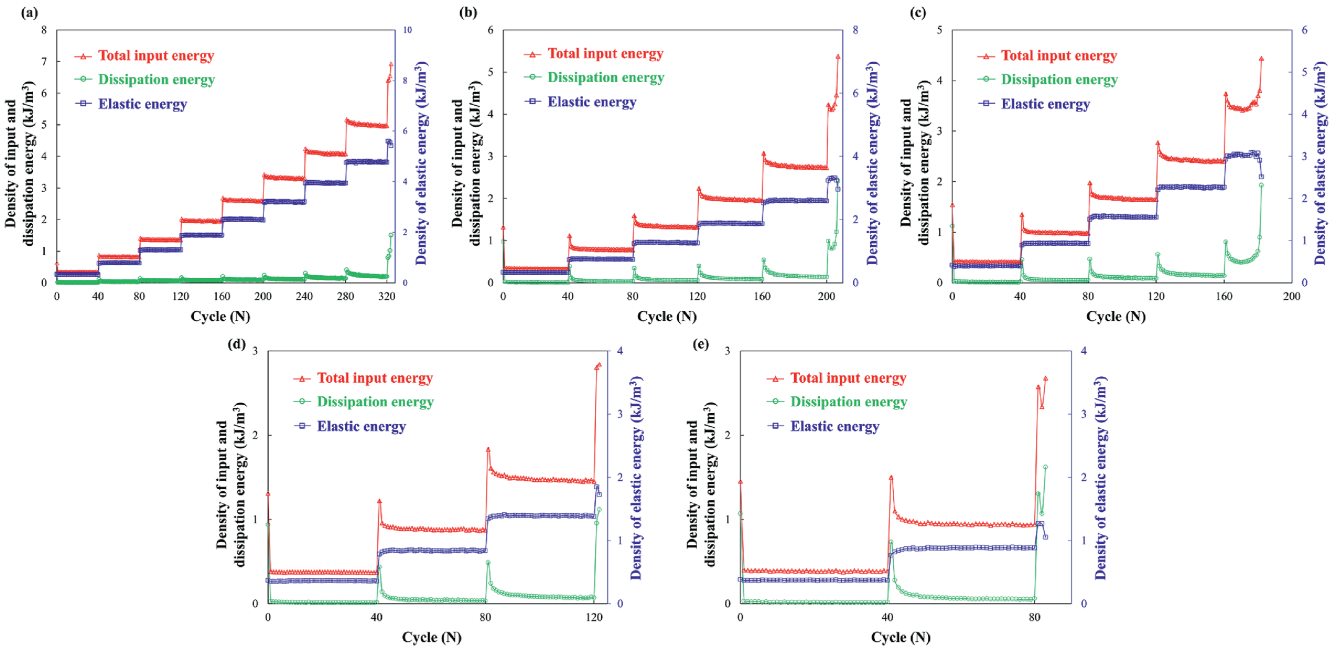

Fig. 15. Energy evolution pattern of marble subjected to varying numbers of thermal cycles under MVF test.

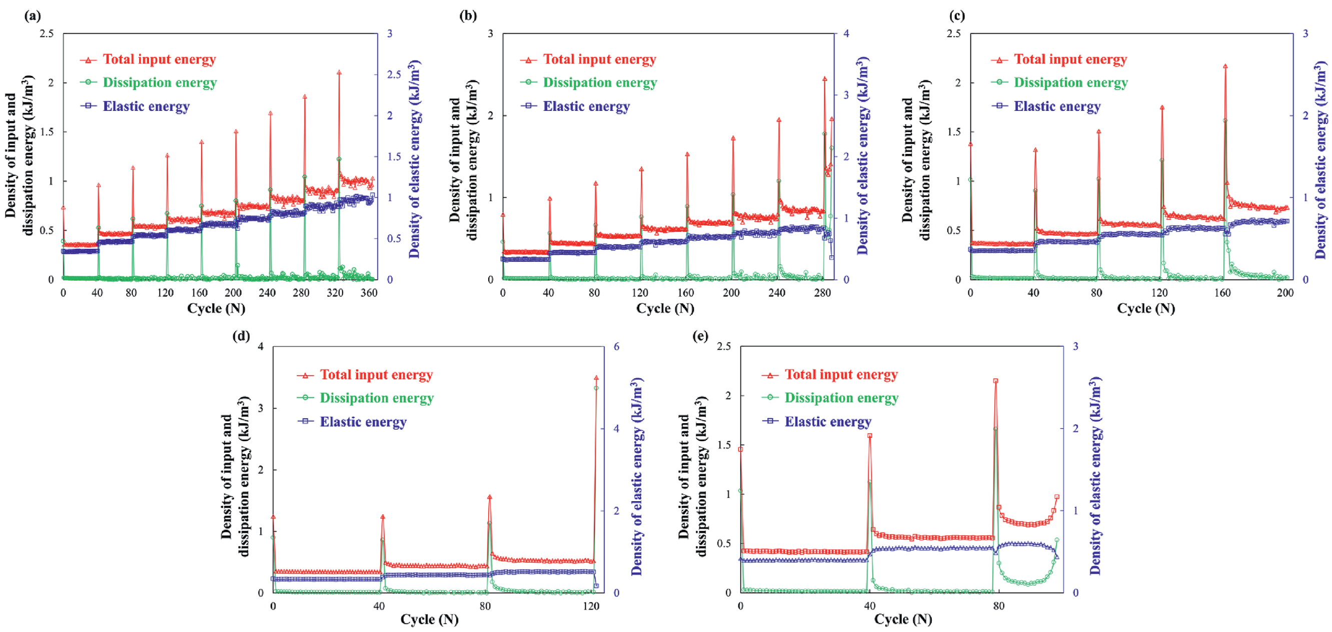

Fig. 16. Energy evolution pattern of marble subjected to varying numbers of thermal cycles under MEF test.

$$D = D_f + D_m - D_f D_m \tag{15}$$

$$D = 1 - \exp\left[-\left(\frac{\gamma_d}{T_0}\right)^{m_0}\right]\left[1 - \sum_{i=1}^{n}\left(\frac{\varepsilon_{ri}}{\varepsilon_m}\right)\right] \tag{16}$$

5.2.4. *Damage constitutive equation and parameter solution*

Based on the above assumption of loss of partial deformation and according to Hooke's law and deformation co-ordination principle, the positive stress of marble can be obtained from the following equation:

$$\sigma_i = E_T \varepsilon_i (1 - D)(1 - e) + \mu\left(\sigma_j + \sigma_k\right) \tag{17}$$

where σ_i is the equivalent stress; i = 1, 2, 3; σ_j and σ_k are the principal stresses in the other directions, respectively, j = 1, 2, 3; k = 1, 2, 3; μ is Poisson's ratio.

Combining Eq. (6), then the maximum and minimum principal stresses can be expressed as

$$\sigma_1 = E_T\left(\varepsilon_1 - \frac{e-e_0}{1-e_0}\right)(1-D)(1-e) + 2\mu\sigma_3 \tag{18}$$

$$\sigma_3 = E_T\left(\varepsilon_3 - \frac{e-e_0}{1-e_0}\right)(1-D)(1-e) + \mu(\sigma_1+\sigma_3) \tag{19}$$

Subtracting equation (14) from equation (15) gives the damage constitutive equation:

$$\sigma_1 - \sigma_3 = \frac{E_T(\varepsilon_1-\varepsilon_3)(1-D)(1-e)}{1+\mu} \tag{20}$$

For the conventional triaxial compression test, only the stress damage caused by monotonic loading is considered, and the damage constitutive equation for the triaxial compression test can be obtained by taking Eq. (16) and Eq. (6) into Eq. (20):

$$\sigma_1 - \sigma_3 = \frac{E_T(\varepsilon_1-\varepsilon_3)\exp\left[-\left(\frac{\gamma_d}{T_0}\right)^{m_0}\right]\left[1-\left(1+\frac{\gamma_d}{\gamma_m^d}\right)\left(\frac{e_0-\varepsilon_v}{1-\varepsilon_v}\right)\right]}{1+\mu} \tag{21}$$

Similarly, for the MEF and MVF stress paths, the damage eigenequation expression is

$$\sigma_1 - \sigma_3 = \frac{E_T(\varepsilon_1-\varepsilon_3)\exp\left[-\left(\frac{\gamma^d}{T_0}\right)^{m_0}\right]\left[1-\sum_{i=1}^{n}\left(\frac{\varepsilon_{ri}}{\varepsilon_m}\right)\right]\left[1-\left(1+\frac{\gamma_d}{\gamma_m^d}\right)\left(\frac{e_0-\varepsilon_v}{1-\varepsilon_v}\right)\right]}{1+\mu} \tag{22}$$

In this study, confining pressure $\sigma_3 = 0$. During multi-stage fatigue loading, the slope of the envelope of the stress-strain curve at each fatigue stage is kept zero, therefore, the following relationship is obtained by the extreme value method:

$$\sigma_{1c} = \frac{E_T(\varepsilon_{1c}-\varepsilon_{3c})\exp\left[-\left(\frac{\gamma_c^d}{T_0}\right)^{m_0}\right]\left[1-\sum_{i=1}^{n}\left(\frac{\varepsilon_{ri}}{\varepsilon_m}\right)\right]\left[1-\left(1+\frac{\gamma_c^d}{\gamma_m^d}\right)\left(\frac{e_0-\varepsilon_{vc}}{1-\varepsilon_{vc}}\right)\right]}{1+\mu} \tag{23}$$

$$\frac{\partial(\sigma_1)}{\partial(\varepsilon_1-\varepsilon_3)} = 0 \tag{24}$$

where σ_{1c} is the axial stress at peak point; ε_{1c}, ε_{3c}, ε_{vc}, γ_c^d are the axial strain, lateral strain, volume strain and plastic deviatoric strain at peak point during MEF and MVF.

The Weibull distribution parameters m_0 and T_0 are obtained by differential solution:

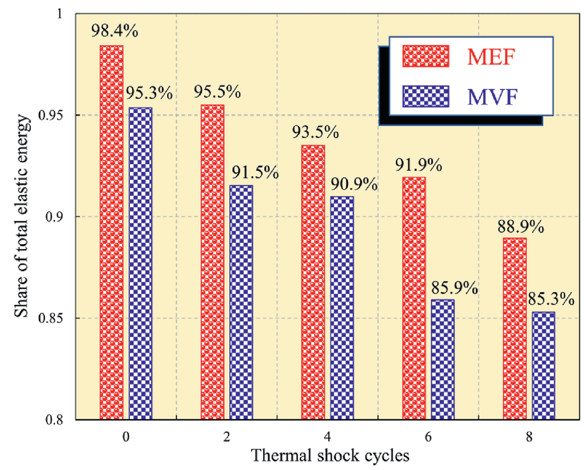

Fig. 17. Total elastic energy shares of marble subjected to varying numbers of thermal cycles under two stress paths.

$$m_0 = \frac{\frac{\gamma_c^d}{(\varepsilon_{1c}-\varepsilon_{3c})} + \frac{-\frac{\gamma_c^d}{\gamma_m^d}\left(\frac{e_0-\varepsilon_{vc}}{1-\varepsilon_{vc}}\right)}{\left[1-\left(1+\frac{\gamma_c^d}{\gamma_m^d}\right)\left(\frac{e_0-\varepsilon_{vc}}{1-\varepsilon_{vc}}\right)\right]} + \frac{-Q\left(1+\frac{\gamma_c^d}{\gamma_m^d}\right)\left(\frac{e_0-1)}{(1-\varepsilon_{vc})^2}\right)}{\left[1-\left(1+\frac{\gamma_c^d}{\gamma_m^d}\right)\left(\frac{e_0-\varepsilon_{vc}}{1-\varepsilon_{vc}}\right)\right]}}{-\ln\frac{(1+\mu)\sigma_{1c}}{E_T H\left[1-\left(1+\frac{\gamma_c^d}{\gamma_m^d}\right)\left(\frac{e_0-\varepsilon_{vc}}{1-\varepsilon_{vc}}\right)\right](\varepsilon_{1c}-\varepsilon_{3c})}} \tag{25}$$

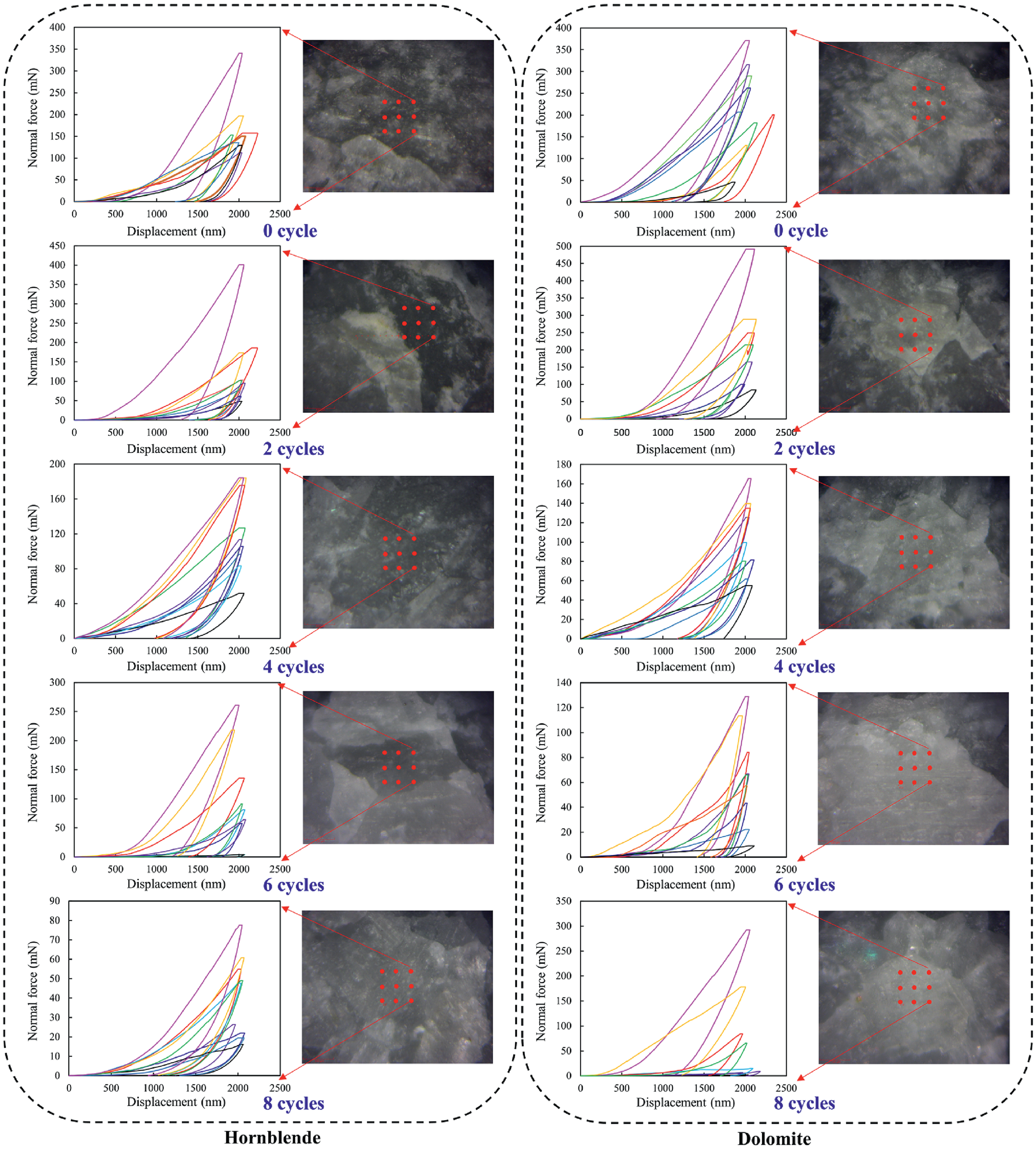

Fig. 18. DSI mechanical curves and microscopic observation graphs of hornblende and dolomite subjected to varying numbers of thermal cycles.

$$T_0 = \frac{\gamma_c^d}{\left[-\ln\dfrac{(1+\mu)\sigma_{1c}}{E_T H\left[1-\left(1+\frac{\gamma_c^d}{\gamma_m^d}\right)\left(\frac{\varepsilon_0-\varepsilon_{vc}}{1-\varepsilon_{vc}}\right)\right](\varepsilon_{1c}-\varepsilon_{3c})}\right]^{\frac{1}{m_0}}} \tag{26}$$

where $Q = \frac{\frac{\partial \varepsilon_v}{\partial(\varepsilon_1-\varepsilon_3)}}{\frac{\partial \gamma^d}{\partial(\varepsilon_1-\varepsilon_3)}}$, $H = E_T\left[1 - \sum_{i=1}^{n}\left(\frac{\varepsilon_{ri}}{\varepsilon_m}\right)\right]$, and the detailed derivation processes are given in Appendix A.

5.3. Validation of H-M damage constitutive model

By combining the experimental results with Eqs. (25) and (26), the model parameters for marble under MVF and MEF loading, subjected to different numbers of thermal cycles, are calculated. The results are presented in Table 2, and the comparisons of the obtained multi-stage fatigue envelopes with the experimental data are shown in Figs. 23 and 24.

As shown in Table 1, since the Poisson's ratio in the fatigue loading stage changes with the number of stages, in order to simplify the calculations, the Poisson's ratio derived from the 30%–70% peak stress segment of the conventional triaxial compression test's stress-strain curve is adopted as a

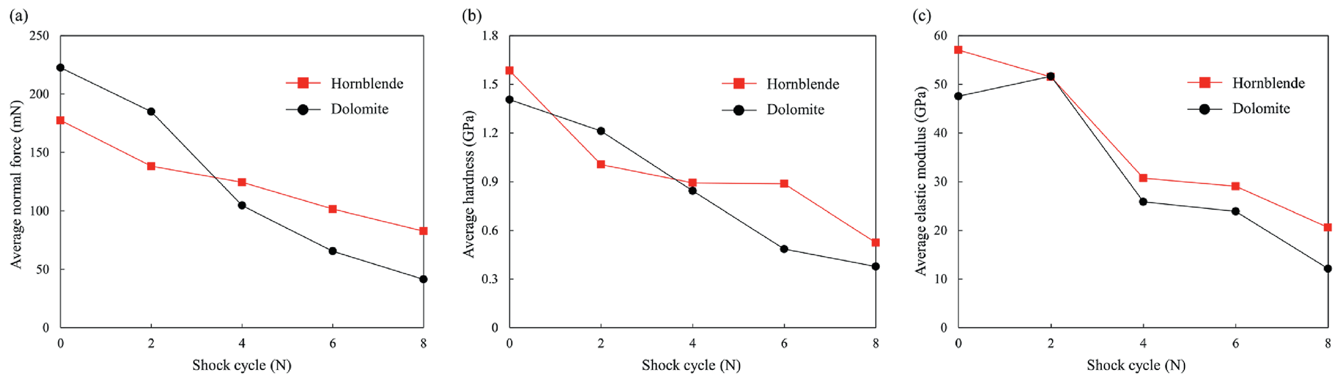

Fig. 19. Variation of (a) average normal load, (b) hardness and (c) elastic modulus for two minerals subjected to varying numbers of thermal cycles under DSI.

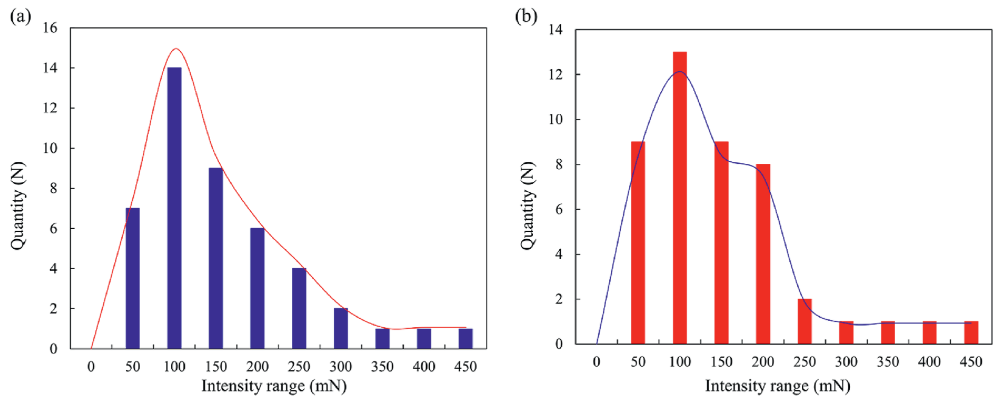

Fig. 20. Distribution of NMR peak intensities in different intensity ranges: (a) dolomite and (b) hornblende.

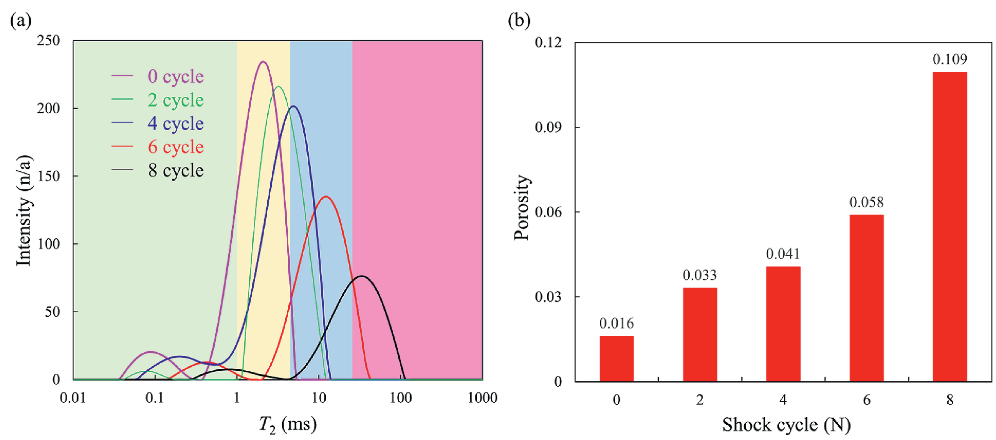

Fig. 21. (a) T_2 distribution curve of marble subjected to varying numbers of thermal cycles, and (b) Evolution of total porosity of marble subjected to varying numbers of thermal cycles.

representative value for both MVF and MEF stages. In addition, since the peak plastic deflection strain in the fatigue process is different in each stage, the extreme values are solved for multiple stages, and Table 1 only lists the distribution parameters of the first stage. In rock mechanics, m_0 indicates the inhomogeneity of the material. the larger the value of m_0, the more discrete the distribution of microcracks within the rock and the more significant the inhomogeneity. In addition, T_0, which represents the characteristic lifetime of a rock specimen, directly quantifies the material's resistance to damage, where higher value is associated with greater resistance to damage and longer life expectancy. The pattern of change in these distribution parameters is conditionally dependent and needs to be analyzed in conjunction with specific experimental conditions, material properties, and external thermal loading strategies (Sun et al., 2020). For example, previous studies have shown that m_0 values typically increase due to microcrack expansion in mechanical cyclic impacts (without thermal action), and that m_0 values may decrease due to weakened mineral particle bonding (with a temporary increase in homogeneity) in thermal cycling (Lu TC. et al., 2024; Yao et al., 2023). In

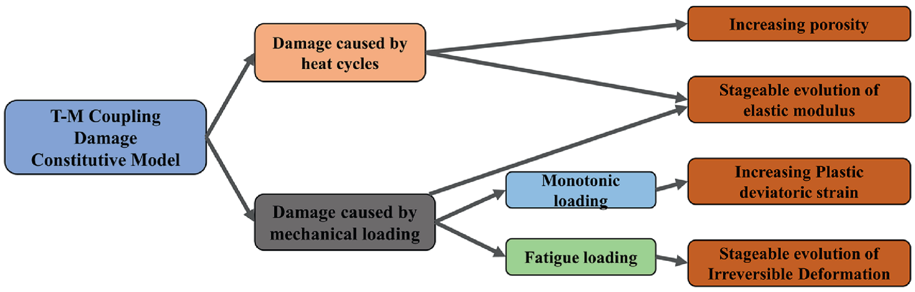

Fig. 22. Flow chart of constitutive equation for thermal-mechanical coupling damage.

Table 2
Modelling parameters of marble subjected to varying numbers of thermal cycles under two loading methods (m_0 and T_0 are the parameters corresponding to the first stage).

Paths	Number of thermal cycles	μ	e_0	γ_m^d	m_0	T_0
MVF	0	0.25	0.016	0.008	0.8760	0.0054
	2	0.26	0.033	0.0156	0.7796	0.0041
	4	0.28	0.041	0.0202	0.7267	0.0029
	6	0.31	0.058	0.0262	0.6410	0.0023
	8	0.35	0.109	0.0324	0.6318	0.0019
MEF	0	0.25	0.016	0.0076	0.825	0.0043
	2	0.26	0.033	0.0162	0.7776	0.0039
	4	0.28	0.041	0.0197	0.7418	0.0036
	6	0.31	0.058	0.0238	0.6733	0.0035
	8	0.35	0.109	0.0287	0.6376	0.0021

this study, as shown in Table 1, the parameters m_0 and T_0 gradually decrease with the increasing number of thermal cycles (m_0 always remains below 1), which implies that the failure mode of the marble specimens after thermal cycles is controlled by the initial defects, and that the rock gradually changes from brittle to ductile with the increasing number of thermal cycles, and both the damage resistance and the fatigue life resistance decrease.

Figs. 23 and 24 present the comparison between the outer envelope lines derived from the thermal-mechanical coupling damage constitutive model and the corresponding experimental curves. The model demonstrates a strong capability to accurately describe the stress-strain envelope of marble subjected to multi-stage fatigue following various thermal cycles. However, the parameters m_0 and T_0, which varied at different stress levels, introduce complexity into the calculation process, thereby restricting the model's applicability.

6. Discussion

6.1. Comparison with existing studies

Compared to existing studies, the innovation of this research is manifested in four key aspects: engineering context, temperature mechanism, stress path and auxiliary monitoring means. As

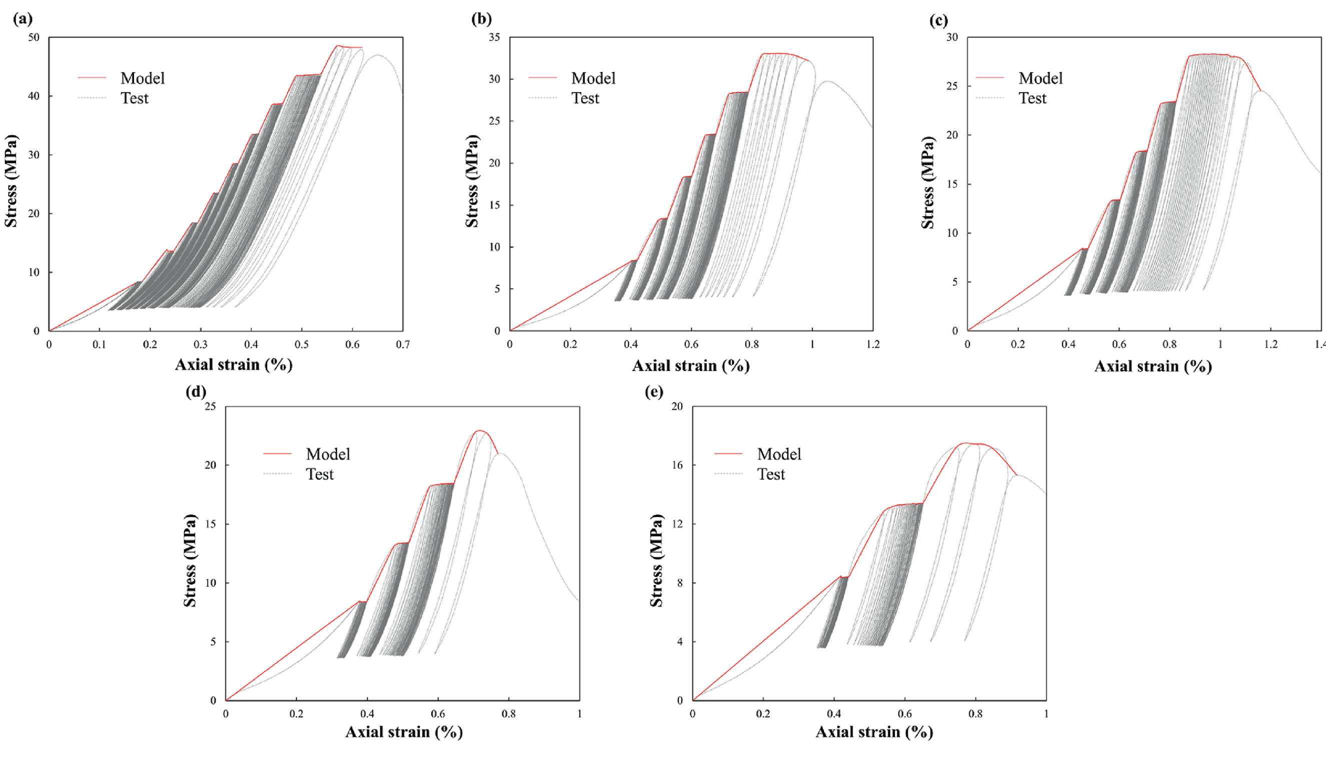

Fig. 23. Comparison of model envelopes and experimental results for marble subjected to varying numbers of thermal cycles under MVF stress path: (a) 0 cycle, (b) 2 cycles, (c) 4 cycles, (d) 6 cycles, and (e) 8 cycles.

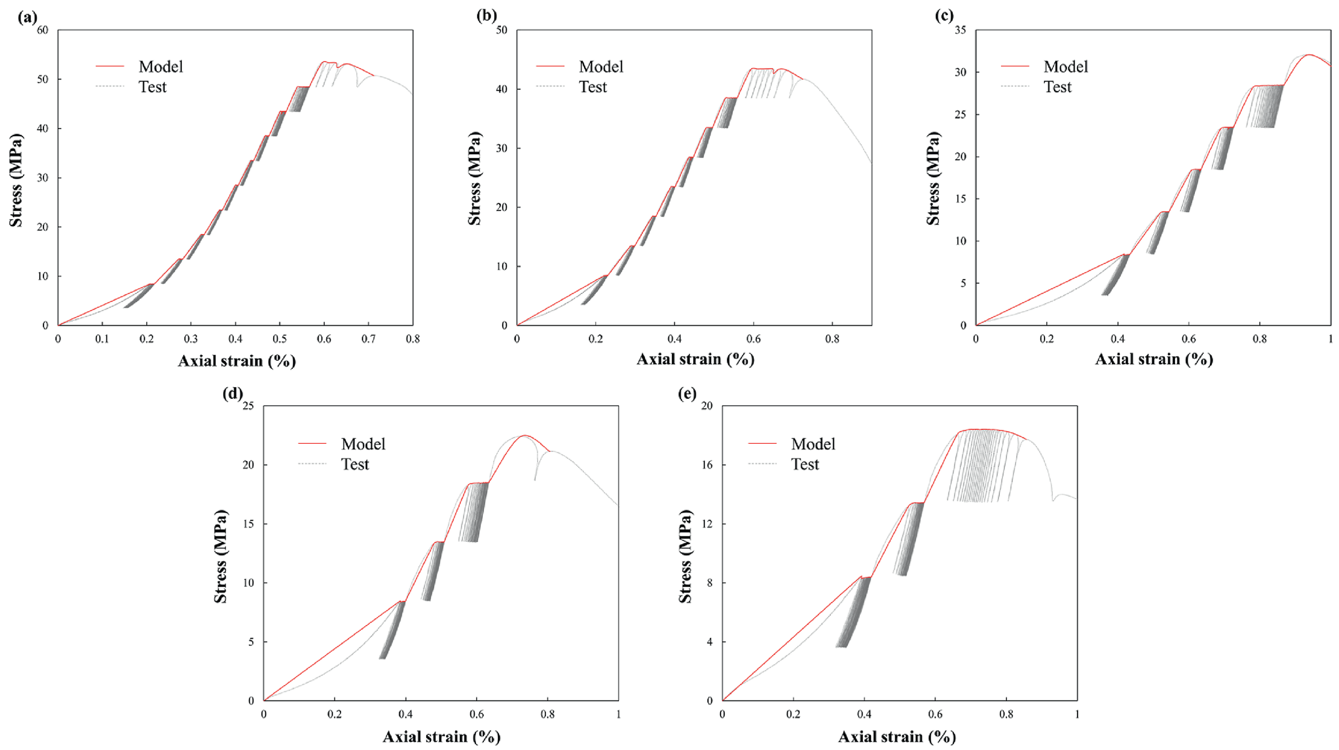

Fig. 24. Comparison of model envelopes and experimental results for marble subjected to varying numbers of thermal cycles under MEF stress path: (a) 0 cycle, (b) 2 cycles, (c) 4 cycles, (d) 6 cycles, and (e) 8 cycles.

shown in Table 3, regarding engineering context, previous studies primarily focused on deep geothermal engineering (typically >300 °C), nuclear waste storage (>400 °C), and thermo-mechanical coupling in ultra-deep tunnels or mining (Liu et al., 2020; Pathiranagei and Gratchev, 2022). In contrast, this work specifically addresses the moderate temperature conditions (<300 °C) prevalent in EGS development. It is noteworthy that the actual thermal cycling amplitude sustain by rock masses during cyclic injection-production in HDR reservoirs is substantially lower than in conventional high-temperature rock engineering scenarios. This fundamental difference governs distinct mineral phase transition mechanisms and thermal damage evolution pathways.

For temperature mechanism, although existing studies have confirmed mechanical degradation of rocks under high temperatures (>300 °C), the mechanical response within the critical 200–300 °C range remained controversial. Some studies reported strength enhancement due to mineral expansion, whereas our experiments revealed that marble subjected to 2, 4, 6, and 8 thermal cycles in this temperature range showed UCS reductions of 22.72%, 43.43%, 53.17%, and 61.29%, respectively, with elastic modulus degradation rates reaching 23.81%, 58.57%, 61.02%, and 68.3%. Besides, it is worth mentioning that Zhou et al. (2015) investigated thermal cycling tests of rocks in the temperature interval from 25 °C to 60 °C and found that some rocks were damaged and showed weakening of the elastic modulus, while some showed strengthening behavior. This suggests that differences in temperature action intervals may lead to different thresholds of strengthening and weakening transformations of rocks. Thermal cycling in the low-temperature interval (<100 °C) may reduce microcracking through thermal compaction effects, and mineral particle expansion differences begin to dominate in the mid-temperature interval (100 °C–300 °C), when the strengthening effect tends to be in a critical state. Whereas the temperature used in the present study, 300 °C, shows a clear tendency to weakening. Furthermore, the thermal cycling amplitude in the high-temperature interval exceeds the critical value, and the damage in the high-temperature interval tends to be irreversible compared to the reversibility of the damage in the low-temperature interval. On the other hand, low amplitude thermal cycling, as well as low-frequency loading, was used in Zhou's study, which may have led to a more pronounced interlocking effect of the particles due to thermal expansion, thus stimulating the hardening mechanism. In contrast, the high-frequency loading, as well as the high-amplitude thermal cycling used in this study, accelerated the concentration of thermal stresses at the crystal interface and widened the range of influence of irreversible thermal damage.

Concerning stress paths, most existing thermo-mechanical coupling tests adopted static monotonic loading (Liu et al., 2020; Pathiranagei and Gratchev, 2022; Fan et al., 2024), failing to replicate the progressive cyclic loading characteristics during hydraulic fracturing. This study adopts MEF and MVF stress paths. Experimental results demonstrate that specimens undergoing 8 thermal cycles exhibit 33.71% and 23.86% higher axial strain accumulation under MVF and MEF loading, respectively, compared to static conditions. This provided critical parameters for evaluating long-term stability of EGS reservoirs under combined fracturing-injection operations.

Ultimately, in terms of auxiliary monitoring methods, existing studies mainly employed P-wave velocity test, XRD and SEM to qualitatively analyze the thermal damage effects (Xiao et al., 2021a,b; Fu et al., 2024; Yu et al., 2025). The P-wave velocity test, for instance, only reflects the changes in the physical properties of macroscopic rocks, and is unable to differentiate between pore evolution and microcrack expansion, the decrease in P-wave velocity after thermal cycling of rock may originate from either increased porosity or grain boundary debonding. Moreover, XRD

Table 3
Existing studies of thermal-mechanical coupling experiments and damage constitutive models.

Background	Experimental content	Complementary means	Rock type	Damage models	Parameter's characteristics	Major conclusion	Reference
Deep geothermal engineering	Monotonic loading after single thermal treatment	EFM codes DEM simulation	Unmentioned	$D_s = \begin{cases} E_0 & F_1<0 \text{ and } F_2<0 \\ E_0 * \left\lvert\frac{\varepsilon_{t0}}{\varepsilon_3}\right\rvert^l & F_1=0 \text{ and } dF_1>0 \\ E_0 * \left\lvert\frac{\varepsilon_{c0}}{\varepsilon_1}\right\rvert^l & F_2=0 \text{ and } dF_2>0 \end{cases}$	ε_1 and ε_3 are the major and minor principal strains. ε_{t0} and ε_{c0} are the maximum tensile and maximum compressive principal strains when tensile and shear damage occurs	The strength and elastic modulus of the rock conform to different damage laws. Numerical results demonstrate that thermally-induced damage is dominated by tensile damage.	Liu et al. (2020)
Underground tunnelling and mining		–	Sandstone	$D = 1-\frac{E_T}{E_0}\exp\left[-\left(\frac{\frac{1}{3}I_1' \sin\varphi - \frac{1}{\sqrt{3}}\sin\varphi\sqrt{J_2'}}{F_0}\right)^m\right]$	F_0 and m are the derived constants I_1' and J_2' defines the first effective stress invariant and the second effective deviator stress invariant, respectively.	The critical thermal damage curve increases polynomially with increasing temperature, while the critical mechanical damage curve shows a gradual decrease.	Pathiranagei and Gratchev (2022)
Opencast mining, tunnel boring or drilling	Monotonic loading after cyclic thermal treatment	P-wave test Diffraction of X-rays (XRD)	Mudstone	$D = \int_{-\infty}^{k}\frac{1}{x\sqrt{2\pi}S_0}\exp\left\{-\frac{1}{2}\left(\frac{\ln k - F_0}{S_0}\right)^2\right\}dx$	F_0 and S_0 are the derived constants The strength limit of the microelements obeys a lognormal distribution.	The temperature dictates the failure modes of rocks, whereas the number of heating and water-cooling cycles influences the crack extension patterns.	Fu et al. (2024)
compressed air energy storage (CAES)		P-wave test	Granite	$D_n = a\sigma_s e^{-\frac{b}{n}} + cT_r - acT_r\sigma_s e^{-\frac{b}{n}}$	a, b and c are derived constants. $\sigma_s=(\sigma_{max}-\sigma_{min})/\sigma_3$, σ_{max} and σ_{min} are the upper and lower limits of cyclic stress, respectively. T_r is the relative temperature variation.	Temperature lowers the fatigue threshold while confining pressure raises it.	Yu et al. (2025)
Nuclear waste storage	Cyclic loading after single heat treatment	NMR	Granite	–	–	As the cyclic number increases, the maximum pore size and porosity decrease first and then increase as the cyclic number increases.	Fan et al. (2024)
Underground coal gasification		Scanning Electron Microscope (SEM)	Sandstone	–	–	Temperature affects the deformation properties of rocks, resulting in a significant correlation between crack volume strain and temperature.	Xiao et al. (2021)
CAES	Cyclic loading after cyclic heat treatment		Basalt	Hardening: $D_n = a_0\Delta T^* e^{-b0/m} - c_0(\delta\overline{\sigma})e^{-d_0/n}$ Weakening: $D_n = \frac{D_n\left(\overline{\sigma}_{max}^b - \overline{\sigma}_{min}^b\right)n^{1-c}}{M\left[1-(1-D_n)^{1+b}\right]} + a_0\Delta T^* e^{-b0/m}$ Total damage: $D_m = (1-D_n)\exp\left[-(F^*/F_0)^m\right]$	$\delta\overline{\sigma} = (\sigma_{max}-\sigma_{min})/UCS$ $\Delta T* = (T_{max}-T_{min})/T_{max}$ $F^* = \sigma_1^* - \frac{(1+\sin\varphi)}{(1-\sin\varphi)}\sigma_3^*$ a_0, b_0, c_0, b, c, M and d_0 arederived constants;	The effect of cyclic temperature can be superposed on the effect of cyclic stress.	Zhou et al. (2015) Zhou et al. (2017)
HDR		NMR DSI	Marble	Damage caused by mechanics: $D = 1 - exp\left[-\left(\frac{\gamma_d}{T_0}\right)^{m_0}\right]\left[1-\sum_{i=1}^{n}\left(\frac{\varepsilon_{ri}}{\varepsilon_m}\right)\right]$ Damage resulted by thermal: $e = \left(1+\frac{\gamma^d}{\gamma_m^d}\right)\left(\frac{e_0-\varepsilon_v}{1-\varepsilon_v}\right)$	m_0, T_0, e_0, μ, γ_m^d are derived constants; Most parameters enjoy natural physical meaning.	The difference in the number of thermal cycles is better reflected in the porosity. Microunit strength of marble after thermal damage conforms to the Weibull distribution.	This study

only provides the mineral phase transition with the volume-averaged information (e.g., 5% decrease in calcite content), while SEM is limited to the observation of surface micrometer-scale morphology (e.g., crack width statistics on grain surfaces). All of these methods lack quantitative correlation between thermal damage and mechanical properties. In this study, we quantitatively resolved the variations in pore structure using NMR to fundamentally quantify the thermal cycling damage. And quantitatively measured the distribution characteristics of hardness, elastic modulus, and strength of the mineral structure at the nanoscale by DSI, which enables the analysis of the damage mechanism from the single-scale observation to the cross-scale.

6.2. Advantages and limitations of the proposed damage model

As shown in Table 3, the damage constitutive models for the four thermal-mechanical coupled cases (monotonic loading after single heat treatment, monotonic loading after cyclic heat treatment, cyclic loading after single heat treatment, and cyclic loading after cyclic heat treatment, respectively) are summarized, and the applications of these models range from different rock types, with or without confining pressure, different stress paths (including amplitude, frequency, and loading modes) to variable thermal paths (including different cooling modes, monotonic heat treatment and cyclic heat treatment) (Zhou et al., 2015, 2017; Liu et al., 2020; Pathiranagei and Gratchev, 2022; Fu et al., 2024; Yu et al., 2025).

In general, these damage models usually distinguish between thermal and mechanical damage, and then the couple both damages to characterize the total damage according to the corresponding geometrical relationships within the microunits. Simultaneously, a commonly accepted assumption is that the distribution of microscopic cracks in rocks is random and that the mechanical damage in rocks can be characterized by a variety of statistical methods, most commonly the Weibull and normal distributions. However, these studies seldom provide an explanation for why adopting these probability distribution functions. In fact, different rock types have different strength distribution characteristics within their micro-element under different temperature environments. This study, however, derives the conclusion by statistically determining the micro-strength through DSI, demonstrating that the Weibull distribution aligns consistently with the experimental results. In addition, in previous studies, many parameters of rocks, such as axial strain, microcrack radius, and energy-elastic modulus, have been treated as randomly distributed variables to define the occurrence of damage. However, these variables tend to neglect thermal damage as well as irreversible deformations caused by fatigue damage.

In defining thermal damage, researchers have focused on changes in macroscopic elastic modulus. Complex empirical models (e.g., S-type or logarithmic) have been used to describe the weakening or strengthening of the elastic modulus due to thermal damage. However, at the microscopic scale, the evolution of macroscopic elastic modulus is fundamentally driven by changes in pore structure and microunit strength. Therefore, based on NMR and DSI experimental results, we developed a damage model incorporating real-time porosity changes. This model yields experimentally accessible invariants that may hold greater practical physical significance than those in previous studies.

The proposed model exhibits three principal limitations that warrant further investigation: (1) Its parametrization relies on multiple experimentally determined parameters, imposing higher data acquisition demands compared to conventional phenomenological models; (2) The formulation lacks capability in capturing thermally induced strength enhancement behavior under specific thermal regimes; (3) The constitutive framework is strictly confined to compressive stress states, failing to characterize tensile modulus degradation and fracture patterns in post-thermal-cycling scenarios.

7. Conclusions

A series of multistage equal-amplitude and variable-amplitude fatigue loading tests were carried out on marble subjected to different numbers of thermal cycles, aiming to deeply explore the mechanical strength, deformation behavior, and the deterioration mechanism of thermal cycles. Micro-mechanical tests including NMR and DSI were conducted to quantify the damage induced by thermal and mechanical stress. The corresponding damage constitutive model under the coupled thermal cycling and fatigue loading conditions was established. The conclusions were summarized as follows:

(1) Reversible deformation distinguished the deformation characteristics of marble under both MVF and MEF loading conditions. Specifically, the reversible deformation corresponding to each cycle increased gradually with the number of stages in MVF while it decreased in MEF.
(2) Under both MEF and MVF loading, the secant modulus increased incrementally with the rising stress level but decreased significantly as thermal cycles accumulated. Additionally, when thermal cycles exceeded six, the deformation modulus of marble transitioned from curvilinear to linear growth.
(3) The DSI results revealed that the mechanical behavior of microunits varied significantly among minerals and locations but generally followed a Weibull distribution. As thermal cycles accumulated, inter- and transgranular cracking increased, whereas the elastic modulus, hardness, and strength of hornblende and dolomite decreased.
(4) The NMR results demonstrated that increasing thermal cycles caused a rightward shift in the T2-curve, revealing a microporosity-to-macroporosity transformation in the marble's pore structure. The measured porosities at 0, 2, 4, 6 and 8 thermal cycles were 1.6%, 3.3%, 4.1%, 5.8% and 10.9% respectively.
(5) Based on the results of macroscopic and microscopic mechanical tests, a damage constitutive model for the coupled action of thermal and mechanical cycles was established using the statistical theory of damage. The model can describe the mechanical characteristics caused by the rock porosity and volume changes under thermal and fatigue loading conditions.

CRediT authorship contribution statement

Yu Song: Writing – original draft, Data curation, Writing – review & editing, Funding acquisition, Methodology, Conceptualization. **Shengqi Yang:** Project administration, Supervision, Funding acquisition. **Kesheng Li:** Supervision, Data curation, Writing – review & editing, Investigation, Methodology, Conceptualization. **Yue Li:** Investigation. **De'an Zheng:** Conceptualization, Investigation, Methodology. **Yanhua Huang:** Investigation.

Data availability statement

Data available upon request.

Declaration of competing interest

The authors declare that they have no known competing financial interests or personal relationships that could have appeared to influence the work reported in this paper.

Acknowledgements

The authors gratefully acknowledge the financial support from the Graduate Innovation Program of China University of Mining and Technology (Grant No. 2024WLKXJ192), the Postgraduate Research & Practice Innovation Program of Jiangsu Province (Grant No. KYCX24_2813).

Appendix A. Supplementary data

Supplementary data to this article can be found online at https://doi.org/10.1016/j.jrmge.2025.06.042.

References

AbuAisha, M., Loret, B., Eaton, D., 2016. Enhanced geothermal systems (EGS): hydraulic fracturing in a thermo-porelastic framework. J. Petrol. Sci. Eng. 146, 1179–1191.
Balbay, A., Esen, M., 2010. Experimental investigation of using ground source heat pump system for snow melting on pavements and bridge decks. Sci. Res. Essays 5 (24), 3955–3966.
Chen, Y.J., Yin, T.B., Wu, Y., 2021. Experimental investigation on dynamic mechanical behavior and fracture evolution of fissure-filled red sandstone after thermal treatment. Eng. Geol. 295, 106433.
Chen, Y.L., Ni, J., Azzam, R., 2012. Experimental study on the influence of temperature on the mechanical properties of granite under uni-axial compression and fatigue loading. Int. J. Rock. Mech. Min. 56, 62–66.
Ebeling, J.C., Kabelac, S., Kruse, H., 2017. Simulation and experimental validation of a 400 m vertical CO_2 heat pipe for geothermal application. Heat. Mass. Transfer. 53 (11), 3257–3265.
Fan, L.F., Wang, Z., Qiu, B., Wang, M., 2024. Evolution of mechanical properties and microstructure in thermally treated granite subjected to cyclic loading. Fatigue. Fract. Eng. M. 47 (4), 1431–1444.
Fu, H.Y., Yu, X.W., Zeng, L., Luo, J.T., Liu, J., 2024. Mechanical properties and damage constitutive model of silty mudstone under heating and water-cooling cycles. Acta Geotech 19 (8), 5031–5050.
Gao, Y., Yu, Z.X., Liu, Y.M., 2024. Metal intrusion enhanced deep learning-based high temperature deterioration analysis of rock materials. Eng. Geol. 335, 107534.
Hu, B., Hu, X.Q., Li, K.H., 2023. Evolution of physical and mechanical properties of granite after thermal treatment under cyclic uniaxial compression. Sustainability 15 (18), 13676.
Huang, W.B., Cao, W.J., Jiang, F.M., 2018. A novel single-well geothermal system for hot dry rock geothermal energy exploitation. Energy 162, 630–644.
Kang, F.C., Li, Y.C., Tang, C.A., 2021. Grain size heterogeneity controls strengthening to weakening of granite over high-temperature treatment. Int. J. Rock. Mech. Min. 145, 104848.
Khatib, H., 2012. IEA world energy Outlook 2011-A comment. Energy Policy 48, 737–743.
Li, K.S., Yang, S.Q., Liu, C.X., Zhang, G.L., Chen, Y., Ma, Q., 2023. Mechanical response and microscopic damage mechanism of pre-flawed sandstone subjected to monotonic and multilevel cyclic loading: a laboratory-scale investigation. Int. J. Min. Sci. Techno. 32 (12), 1487–1510.
Li, M., Wang, D.M., Shao, Z.L., 2020. Experimental study on changes of pore structure and mechanical properties of sandstone after high-temperature treatment using nuclear magnetic resonance. Eng. Geol. 275, 105739.
Li, X.F., Zhang, F.S., Xiu, N.L., Weng, D.W., Cai, B., Fu, H.F., 2024. Shear-induced permeability evolution of natural fractures in granite: implications for stimulation of EGS reservoirs. Eng. Geol. 338, 107629.
Liang, W.G., Xu, S.G., Zhao, Y.S., 2006. Experimental study of temperature effects on physical and mechanical characteristics of salt rock. Rock Mech. Rock. Eng. 39 (5), 469–482.
Liu, K.Q., Rassouli, F.S., Liu, B., Ostadhassan, M., 2021. Creep behavior of shale: nanoindentation vs. triaxial creep test. Rock mech. Rock. Eng 54 (1), 321–335.
Liu, L.Y., Ji, H.G., Elsworth, D., Zhi, S., Lv, X.F., Wang, T., 2020. Dual-damage constitutive model to define thermal damage in rock. Int. J. Rock. Mech. Min. 126, 104185.
Liu, W.Y., Zhu, Q.Z., Zhang, J., Song, M., Sun, H.H., 2023. A micromechanical fatigue damage model for quasi-brittle rocks subjected triaxial compressive cyclic loads. Comput. Geotech. 163, 105747.
Lu, T.C., Wu, H., Yin, S.M., Xu, X.L., 2024. Study of rock damage constitutive model considering temperature effect based on Weibull distribution. Appl. Sci. Basel. 14 (9), 3766.
Luo, H., Gong, H.L., Li, X.P., 2024. The macroscopic and microscopic fatigue failure mechanisms of high-temperature thermally-damaged granite under cyclic impact loading. Geothermics 121, 103047.
Luo, J.A., He, J., 2022. Constitutive model and fractured failure of sandstone damage under high temperature-cyclic stress. Materials 15 (14), 4903.
Ma, X., Dong, W.B., Zhou, H., 2023. Mechanical properties of granite at high temperature subjected to true triaxial compression. Int. J. Rock. Mech. Min. 164, 105313.
Meng, Q.B., Liu, J.F., Wang, C.K., 2021. Mechanical properties of limestone after high-temperature treatment under triaxial cyclic loading and unloading conditions. Rock Mech. Rock. Eng 54 (12), 6413–6437.
Meng, Q.B., Liu, J.F., Zhang, Z.Z., 2022. Effects of confining pressure and temperature on the energy evolution of rocks under triaxial cyclic loading and unloading conditions. Rock Mech. Rock Eng. 55 (2), 773–798.
Pathiranagei, S.V., Gratchev, I., 2022. Coupled thermo-mechanical constitutive damage model for sandstone. J. Rock. Mech. Geotech. 14 (6), 1710–1721.
Ren, C.H., Yu, J., Liu, S.Y., Yao, W., Zhu, Y.L., Liu, X.Y., 2022. A plastic strain-induced damage model of porous rock suitable for different stress paths. Rock Mech. Rock Eng. 55 (4), 1887–1906.
Riahi, A., Pettitt, W., Blanksma, D., 2019. Numerical modeling of discrete fractures in a field-scale forge EGS reservoir. Rock Mech. Rock Eng. 52 (12), 5245–5258.
Sepúlveda, J., Arancibia, G., Bracke, R., 2020. Thermo-mechanical behavior of a granodiorite from the Liquine fractured geothermal system (39°S) in the southern volcanic zone of the Andes. Geothermics 87, 101828.
Sheng, M., Li, P., Wang, J.B., 2020. Influence of cyclic normal stress on shear friction of EGS granite fractures. Eng. Fract. Mech. 238, 107268.
Shi, Y., Shen, W.Q., Shao, J.F., 2024. A micromechanics based model for sandstone under monotonic cyclic compression. Int. J. Rock. Mech. Min. 180, 105823.
Shkuratnik, V.L., Kravchenko, O.S., Filimonov, Y.L., 2020. Stress memory in acoustic emission of rock salt samples in cyclic loading under variable temperature effects. J. Min. Sci. 56 (2), 209–215.
Song, Y., Li, K.S., Tian, W.L., 2023. Mechanical response of sandstone exposed to monotonic and multilevel fatigue loading: insights from deformation, energy, and acoustic emission characteristics. Theor. Appl. Fract. Mech. 128, 104181.
Song, Y., Yang, S.Q., Li, K.S., 2024. Experimental investigation on thermal strengthening behaviour of marble in the mild temperature range under cyclic loading. Geothermics 121, 103041.
Sun, B., Yang, P., Zhang, Z.H., Wang, S.Y., Zeng, S., 2024. Investigation of the fracture characteristics of rock mass after thermal-mechanical damage coupling. Rock Mech. Rock. Eng. 57 (7), 4707–4727.
Sun, W., Duan, C.Z., Yin, W.D., 2020. Development of dynamic constitutive model with particle damage and thermal softening for Al/SiCp composites. Compos. Struct. 236, 111856.
Templeton, J.D., Ghoreishi-Madiseh, S.A., Al-Khawaja, M.J., 2014. Abandoned petroleum wells as sustainable sources of geothermal energy. Energy 70, 366–373.
Tian, W.L., Yang, S.Q., Dong, J.P., 2021. Failure behavior of the thermal treated granite under triaxial cyclic loading-unloading compression. Geomech. Geophys. Geo. 7 (1), 19.
Tian, Y.L., Chen, S.W., Zheng, K.X., 2022. Experimental study on thermo-mechanical properties of Beishan granite under mild temperature. Case Stud. Therm. Eng. 37, 102271.
Villarreal, O.R., Valdez, A.V., Rivera, M.H., 2021. Estimation of fracture energy from hydraulic fracture tests on mortar and rocks at geothermal reservoir temperatures. Rock Mech. Rock. Eng 54 (8), 4111–4119.
Waragai, T., 2022. Influence of thermal cycling in the mild temperature range on the physical properties of cultural stones. J. Cult. Herit. 59, 171–180.
White, M., McClure, M., Danko, G., Elsworth, D., Sonnenthal, E., Kelkar, S., Podgorney, R., 2018. A suite of benchmark and challenge problems for enhanced geothermal systems. Geomech. Geophys. Geo. 4 (1), 79–117.
Williamson, K.H., Gunderson, P.R., Hamblin, G.M., Gallup, D.L., Kitz, K., 2001. Geothermal power technology. P. IEEE 89 (12), 1783–1792.
Wong, L.N.Y., Cui, X., Guo, T.Y., 2022. Experimental investigation of thermal strengthening in Sichuan marble. Rock Mech. Rock Eng. 55 (11), 6683–6702.
Wong, L.N.Y., Zhang, Y.H., Wu, Z.J., 2020. Rock strengthening or weakening upon heating in the mild temperature range? Eng. Geol. 272, 105619.
Xiao, W.J., Yu, G., Li, H.T., Zhan, W.Y., Zhang, D.M., 2021a. Experimental study on the failure process of sandstone subjected to cyclic loading and unloading after high temperature treatment. Eng. Geol. 293, 106305.
Xiao, W.J., Zhang, D.M., Yu, B.C., 2021b. Difference analysis on sandstone permeability after treatment at different temperatures during the failure process: a case study of sandstone in Chongqing, China. Pure. Appl. Geophys. 178 (5), 1893–1910.
Yan, J.H., Zeng, Z.F., Zhou, S., Ming, Y.Y., Ren, Z.W., Wang, L.X., An, B.Z., Tan, H.D., Zhao, J.W., 2024. Study on the resistivity structure and geothermal genesis mechanism of Gudui geothermal field in Tibet, China. Geothermics 119, 102929.
Yang, F.B., Chen, S.W., He, Q., 2022. Study on the mechanism of mechanical property strengthening of Beishan granite under mild temperature condition. Case Stud. Therm. Eng. 40, 102554.
Yang, S.Q., Jing, H.W., Jiao, Y.Y., 2014. Fracture mechanical behavior of red sandstone containing a single fissure and two parallel fissures after exposure to different high temperature treatments. J. Struct. Geol. 69, 245–264.
Yao, W., Yu, J., Liu, X.Y., Zhang, Z.Q., Feng, X.W., Cai, Y.Y., 2023. Experimental and theoretical investigation of coupled damage of rock under combined disturbance. Int. J. Rock. Mech. Min. 164, 105355.
Yin, T.B., Li, X.B., Huang, S., 2012. Effect of thermal treatment on the dynamic fracture toughness of Laurentian Granite. Rock Mech. Rock. Eng. 45 (6), 1087–1094.
Yu, Z.Y., Shen, S.W., Li, M., Zhang, M., Tian, L.P., Hua, G.W., 2025. An improved rock damage model from a cyclic temperature-triaxial loading experiment for compressed air energy storage caverns. Eng. Geol. 344, 107857.
Zhang, P., Mishra, B., Heasley, K.A., 2015. Experimental investigation on the influence of high pressure and high temperature on the mechanical properties of deep reservoir rocks. Rock Mech. Rock Eng. 48 (6), 2197–2211.
Zhang, Z.X., Yu, J., Lindqvist, P.A., 2001. Effects of high temperatures on dynamic rock fracture. Int. J. Rock. Mech. Min. 38 (2), 211–225.
Zhong, C.H., Xu, T.F., Li, X., 2023. Coupled effects of elastic and plastic deformation on hydraulic properties of the geothermal fracture induced by cyclic loading-unloading processes. Eng. Geol. 313, 106929.
Zhou, S.W., Xia, C.C., Hu, Y.S., Zhou, Y., Zhang, P.Y., 2015. Damage modeling of basaltic rock subjected to cyclic temperature uniaxial stress. Int. J. Rock. Mech. Min. 77, 163–173.

Zhou, S.W., Xia, C.C., Zhao, H.B., Mei, S.H., Zhou, Y., 2017. Statistical damage constitutive model for rock subjected to cyclic stress and cyclic temperature. Acta Geophys. 65 (5), 893–906.

Prof. Shengqi Yang obtained his BSc and MSc degrees in Mine Construction and Engineering Mechanics from Jiaozuo Institute of Technology (now Henan Polytechnique University), China, in 2000 and 2003, respectively, and his PhD degree in Geotechnical Engineering from Hohai University, China, in 2006. In 2007–2008, he undertook further post-doctoral research at the Ecole Polytechnique de Paris in France. Since December 2008, he has been employed as an Associate Professor at the School of Mechanics and Civil Engineering, China University of Mining and Technology. From January 2012 to July 2024, he held the position of Full-time Professor in the School of Mechanics and Civil Engineering, China University of Mining and Technology. In July 2024, he joined the School of Civil Engineering and became the executive director of the Center of Rock Mechanics and Geohazards, Shaoxing University as a Full-time Professor. In 2014 and 2015, he was awarded an Endeavour Research Fellowship in Australia and commenced his research in the Department of Civil Engineering, Monash University as a visiting professor. Since 2016, he has engaged in a number of international collaborative research projects at Nanyang Technological University, (Singapore), The University of Nottingham (UK), Monash University (Australia), and Imperial College London (UK) as a visiting professor. In 2012, he was awarded the Program for New Century Excellent Talents in University, a grant provided by the Ministry of Education of China. In 2015, he was awarded financial support from the Natural Science Foundation of Jiangsu Province for Distinguished Young Scholars. His research interests cover deep rock mechanics and underground engineering. To date, he has published one Chinese and two English monographs. Additionally, he has published more than 200 peer-reviewed papers and received seven provincial and ministerial-level scientific and technological achievement awards. He was also one of the 2019–2024 Chinese Most Cited Researchers in the field of civil engineering. He has applied for more than 40 national invention patents, of which 34 have been granted. He is an editorial board member of several journals, including “Engineering Geology”, “Rock Mechanics and Rock Engineering”, “Computers and Geotechnics”, “Geomatics, Natural Hazards and Risk” and he is also the associate editor of “Geomechanics and Geophysics for Geo-Energy and Geo-Resources".